Anatomical background and generalized detectability in tomosynthesis and cone-beam CT

G. J. Gang
Institute of Biomaterials and Biomedical Engineering, University of Toronto, Toronto, Ontario M5G 2M9, Canada

D. J. Tward
Department of Biomedical Engineering, Johns Hopkins University, Baltimore, Maryland 21205

J. Lee
Department of Electrical and Computer Engineering, Johns Hopkins University, Baltimore, Maryland 21218

J. H. Siewerdsen[a)]
Institute of Biomaterials and Biomedical Engineering, University of Toronto, Toronto, Ontario M5G 2M9, Canada and Department of Biomedical Engineering, Johns Hopkins University, Baltimore, Maryland 21205

(Received 23 October 2009; revised 1 February 2010; accepted for publication 1 February 2010; published 9 April 2010)

Purpose: Anatomical background presents a major impediment to detectability in 2D radiography as well as 3D tomosynthesis and cone-beam CT (CBCT). This article incorporates theoretical and experimental analysis of anatomical background "noise" in cascaded systems analysis of 2D and 3D imaging performance to yield "generalized" metrics of noise-equivalent quanta (NEQ) and detectability index as a function of the orbital extent of the (circular arc) source-detector orbit.
Methods: A physical phantom was designed based on principles of fractal self-similarity to exhibit power-law spectral density (κ/f^{β}) comparable to various anatomical sites (e.g., breast and lung). Background power spectra [$S_B(f)$] were computed as a function of source-detector orbital extent, including tomosynthesis ($\sim 10^\circ - 180^\circ$) and CBCT ($180^\circ$+fan to 360°) under two acquisition schemes: (1) Constant angular separation between projections (variable dose) and (2) constant total number of projections (constant dose). The resulting S_B was incorporated in the generalized NEQ, and detectability index was computed from 3D cascaded systems analysis for a variety of imaging tasks.
Results: The phantom yielded power-law spectra within the expected spatial frequency range, quantifying the dependence of clutter magnitude (κ) and correlation (β) with increasing tomosynthesis angle. Incorporation of S_B in the 3D NEQ provided a useful framework for analyzing the tradeoffs among anatomical, quantum, and electronic noise with dose and orbital extent. Distinct implications are posed for breast and chest tomosynthesis imaging system design—applications varying significantly in κ and β, and imaging task and, therefore, in optimal selection of orbital extent, number of projections, and dose. For example, low-frequency tasks (e.g., soft-tissue masses or nodules) tend to benefit from larger orbital extent and more fully 3D tomographic imaging, whereas high-frequency tasks (e.g., microcalcifications) require careful, application-specific selection of orbital extent and number of projections to minimize negative effects of quantum and electronic noise.
Conclusions: The complex tradeoffs among anatomical background, quantum noise, and electronic noise in projection imaging, tomosynthesis, and CBCT can be described by generalized cascaded systems analysis, providing a useful framework for system design and optimization. © *2010 American Association of Physicists in Medicine*. [DOI: 10.1118/1.3352586]

Key words: tomosynthesis, cone-beam CT, anatomical noise, anatomical clutter, anatomical background, cascaded systems analysis, noise-power spectrum, noise-equivalent quanta, detectability index, imaging task

I. INTRODUCTION

Image "noise" may be broadly interpreted to describe variations in the image that impede the imaging task, including purely stochastic variations (such as quantum noise) as well as deterministic (or semideterministic) variations such as structured pattern noise, correlated electronic noise, and artifacts of image processing/reconstruction.[1–4] Similarly, anatomical background (i.e., image variations arising from anatomy not associated with the structure of interest) presents a major impediment to detectability in various imaging applications (e.g., breast,[2] chest,[3,5] dental,[6] angiography,[7] and

liver[8]), often outweighing other noise sources, such as quantum or electronic noise.[4] Thus, anatomical background noise presents an important factor to be incorporated in the description of system performance, not only in 2D projection imaging[1,5,9–11] (in which 3D anatomy is entirely superimposed in the 2D image) but also in tomosynthesis (giving partial rejection of out-of-plane structure)[12,13] and cone-beam CT (CBCT) (in which anatomical background is minimized to residual in-plane structure). As detailed below, the latter represents a continuum in the reduction of anatomical background in proportion to the extent of the source-detector angular orbit.

The characterization of anatomical background has been an area of considerable interest in 2D medical imaging applications, such as mammography and chest radiography. For example, Burgess *et al.*[14] described breast structure by an empirical power-law relationship in proportion with κ/f^{β}, with the power-law exponent measured approximately to be 2.8 in digitized film-screen mammograms.[15] Heine *et al.*[16] similarly showed that the statistical nature of mammograms can be depicted by white noise, filtered with a parametric transfer function of the form $1/f^{\beta}$ and measured the value of β to be in the range 2.8–3.0 in digital mammograms.[17] In 2D chest radiography, Samei[3,10] showed the predominance of anatomical background noise over other noise sources, and Richard *et al.*[18] characterized such in terms of power-law noise with β in the range ~3.5–4. Such analysis was subsequently extended to dual-energy chest radiography,[19] where reduction in anatomical noise through tissue discrimination (i.e., the soft-tissue image) was associated with a decreased value of κ and significantly increased detectability.

The power-law depiction of anatomical noise has been extended to 3D imaging applications as well. In the context of breast tomosynthesis and CBCT, for example, Glick *et al.*[20] included an anatomical noise-power spectrum (NPS) in proportion with $1/f^3$ in investigating the optimal scintillator thickness for a CT mammography system, and Gong *et al.*[21] applied the same to simulate a digital breast phantom. Metheany *et al.*[22] extended Burgess' analysis to breast CT, confirming a difference of 1 between β in breast CT slices and mammograms (viz., β=3.01 in projections, β=1.86 in breast CT slices, and β=2.06 in breast CT slices segmented such that adipose and glandular tissue voxels carried values of 1 and 2, respectively). Engstrom *et al.*[23] similarly compared breast tomosynthesis slices and projection data, and found reduced background in tomosynthesis slices evidenced by a lower β (2.87 compared to 3.06). In 3D chest tomosynthesis, Yoon *et al.*[24] measured β and κ in an anthropomorphic phantom and applied the findings to theoretical analysis of detectability as a function of β and κ and extent of the source-detector orbit.

The work described below extends power-law analysis of background clutter to the full continuum of source-detector orbital extent, from a single projection (2D radiograph) to limited arc tomosynthesis and fully 3D CBCT. The work involves experimental analysis based on a physical phantom presenting power-law noise and theoretical analysis of the corresponding detectability index for a variety of imaging tasks. While the phantom is not intended to simulate a particular anatomical site (e.g., breast or chest), the approach offers a general experimental and theoretical basis with specific implications for systems currently under development for diagnostic and image-guided procedures. The study extends 3D cascaded systems analysis of tomosynthesis and CBCT (Ref. 25) to quantify the tradeoffs among anatomical background, quantum, and electronic noise as a function of orbital extent, number of projection views, and dose. The generality as well as the limitations of the current study are addressed, and the implications for site-specific 3D imaging applications (e.g., the breast or chest) are described.

II. METHODS

The theoretical and experimental methods are summarized below. First, an analytical basis drawn from fractal theory is presented for the design of phantoms presenting power-law noise in 2D projections and 3D reconstructions, along with an example phantom constructed of various diameter spheres. Second, image acquisition schemes and methods of signal, noise, and power spectrum measurements are discussed. Finally, a cascaded systems model for tomosynthesis and CBCT is extended to include anatomical background noise in "generalized" description of the NEQ and detectability index.

II.A. Analytical basis and design of a "clutter" phantom for power-law noise

Anatomical background power spectra intrinsic to the object (clutter), denoted as $S_{B-\mathrm{obj}}$ are frequently characterized according to the fairly ubiquitous power-law relationship [Eq. (1)] used to describe a wide range of random and stochastic processes:[26]

$$S_{B-\mathrm{obj}}(f) = \frac{\kappa_{\mathrm{obj}}}{(af)^{\beta_{\mathrm{obj}}}}, \tag{1}$$

where κ_{obj} describes the magnitude of fluctuation, β_{obj} denotes the degree of correlation of the variations, and f is the spatial frequency coordinate. The term a is a scale factor (taken as 1) carrying units inverse to frequency (e.g., a=1 mm for f in units of mm^{-1}), effectively an aperture making the denominator dimensionless despite different values of β_{obj}. Such a power-law characteristic has been used in the empirical description of anatomical background in breast[15,22,23] and chest[24] imaging. In this work, a physical phantom was designed to present the same form of power-law spectral density as found in such anatomical sites (i.e., similar β_{obj}). In this way, the current work is intended as a general analysis of power-law noise in tomosynthesis and CBCT in a manner that is pertinent to various clinical applications, but not specific to any organ in particular.

The phantom design was based on the properties of self-similar objects, a special class of which are fractals. Such objects exhibit power-law spectral density with the exponent β_{obj} related to the fractal dimension by[26]

$$D = E + \frac{\beta_{\text{obj}} - 3}{2}, \tag{2a}$$

$$\beta_{\text{obj}} = 2(D - E) + 3, \tag{2b}$$

where D is the fractal dimension, E is the Euclidean dimension in which the fractal is embedded, and β_{obj} is the power-law exponent of the power spectrum of the object. For example, a 3D object with fractal dimension $D=3$ (e.g., 3D Hilbert curve with fractal dimension defined as the Hausdorff dimension) gives $\beta_{\text{obj}}=3$, which is close to that measured for the breast and chest.[15,22–24] In the current work, for simplicity, we consider objects with 3D symmetrical power spectrum, such as a random collection of spheres. The box-counting method (a means of measuring the fractal dimension) dictates that the number of boxes, denoted N_{l_m}, each of side-length l_m, required to cover the fractal is related to the fractal dimension by[26,27]

$$N_{l_m} \propto \frac{1}{l_m^D}. \tag{3}$$

The number of boxes of size l_m required to cover a sphere of diameter $l_i > l_m$ is equal to the ratio of their volumes l_i^3/l_m^3. Similarly, a box of size l_m can cover l_m^3/l_i^3 spheres of size $l_i < l_m$. Therefore, the number of boxes of size l_m required to cover a tightly packed volume of spheres of different sizes is approximately

$$N_{l_m} = n_{l_m} + \sum_{l_i > l_m} n_{l_i} \times \left(\frac{l_i^3}{l_m^3}\right) + \sum_{l_j < l_m} n_{l_j} \times \left(\frac{l_j^3}{l_m^3}\right), \tag{4}$$

where n_{l_m} is the number of spheres of diameter l_m in the phantom. For N_{l_m} to satisfy Eq. (2) when $D=3$, it follows that

$$n_{l_m} \propto \frac{1}{l_m^3}, \tag{5}$$

which implies that equal volumes of differently sized spheres gives fractal dimension $D=3$ as well as a power-law exponent of $\beta_{\text{obj}}=3$. In principle, higher or lower fractal dimension (and power-law exponent) can be achieved by varying the proportion and density of various size spheres comprising the object, giving a means of experimentally achieving any particular value of β_{obj}.

From this analytical basis for power-law noise, a clutter phantom was constructed of equal volumes of acrylic spheres of five different diameters (15.88, 12.70, 9.52, 6.35, and 3.18 mm), approximating an object with $\beta_{\text{obj}}=3$. An equal volume of each size sphere corresponds to a number of spheres in proportion to 1, 1.95, 4.63, 15.63, and 125, respectively. The spheres were randomly mixed to fill an acrylic box of dimension $(20\times20\times12.5)$ cm^3, as illustrated in Fig. 1. While true self-similarity would require spheres ranging from infinitely small to infinitely large, the physical phantom satisfies self-similarity over a finite spatial frequency range over which the fractal dimension and β_{obj} values are expected to hold. The size of the box was consistent with the 3D field of view of the CBCT imaging bench [Fig. 1(a)]. Alternative containers were also investigated, e.g., a cylinder of diameter ~16 cm. A cylindrical phantom with a well-matched bowtie filter provided uniform quantum noise, but significant nonstationarity in the projection (and low-angle tomosynthesis) power spectrum associated with clutter. For all measurements below, a simple rectangular box was found to be a reasonable choice in that its uniform thickness gave the most spatially uniform attenuation and best overall stationarity in 2D projections and low-angle tomosynthesis images. That is, both the quantum noise and anatomical clutter were more spatially invariant in first-order and second-order statistics for the rectangular box phantom (compared to a cylindrical phantom) given regions of interest (ROIs) sufficiently large to capture the longest-scale fluctuation of interest.

We distinguish between the power spectrum intrinsic to the object $[S_{B-\text{obj}}(f)]$ and that measured in an image of the object $[S_B(f)]$, with $S_B(f)=\text{MTF}^2(f)S_{B-\text{obj}}(f)$, where $\text{MTF}(f)$ is the modulation transfer function of the system. Similarly, κ_{obj} and β_{obj} refer to power-law characteristics in the object domain, while κ and β refer to power-law characteristics in the image domain. As detailed below, the clutter phantom was used to measure the background anatomical power spectrum, $S_B(f_x,f_y,f_z)$ as a function of the acquisition angle, θ_{tot}. While it is generally appreciated that increasing θ_{tot} "rejects" anatomical clutter from slice reconstructions, these measurements provided quantitative analysis of the behavior of power-law characteristics κ and β as a function of θ_{tot}.

II.B. Image acquisition and reconstruction

Images were acquired using an experimental imaging bench designed for tomosynthesis and CBCT from a circular arc source-detector trajectory. As described in previous works,[25,28,29] the bench consists of an x-ray tube (Rad 94 in a sapphire housing; Varian Medical Systems, Salt Lake City, UT), a CsI:TI flat-panel detector (RID-1640A, Perkin Elmer Optoelectronics, Santa Clara, CA), and a motion control system (6 K series translation stages, Parker Daedal, Harrison PA, and Dynaserv rotation motor, Parker Hannifin, Rohnert Park, CA). Images were acquired nominally at 120 kVp (1.53 mm Al+1.1 mm Cu added filtration) and 0.63 mA s per projection, giving in-air exposure of 1.84 mR/mA s at isocenter and 0.49 mR/projection at the flat panel detector (FPD).[30] The bench geometry is illustrated in Fig. 1(a). The (x, y, z) axes are fixed in the 3D object space such that (x, y) refers to the axial plane, (y, z) refers to the sagittal plane, and (x, z) refers to the coronal plane. Specifically, y is the inter-slice "depth" direction in 3D tomosynthesis reconstructions.

In addition to 2D projections ($\theta_{\text{tot}}=0°$), 3D images were reconstructed using the FDK algorithm for 3D filtered back-projection for 15 settings representing the spectrum of tomosynthesis ($\theta_{\text{tot}}=10°$, 20°, 30°, 40°, 50°, 70°, 90°, 120°, 150°, and 180°) and fully 3D CBCT [$\theta_{\text{tot}}=200°$ (180°+fan), 240°, 280°, 320°, and 360°]. For each setting of θ_{tot}, two acquisition schemes were considered: (1) Constant angular separation between projections (subsequently referred to as the "constant-$\Delta\theta$" scheme, with $\Delta\theta=0.45°$), in which case the

TABLE I. Experimental conditions under the constant-$\Delta\theta$ and constant-N_{proj} cases. The exposure values represent total in-air exposure to the detector and total dose approximates the dose to the center of a 10 cm diameter water cylinder placed at isocenter—a rough approximation to the 10 cm clutter phantom. A scatter factor of 4.5 and f-factor of 0.9 was assumed.

	Constant-$\Delta\theta$				Constant-N_{proj}			
θ_{tot} (deg)	$\Delta\theta$ (deg)	N_{proj}	Exposure (mR)	Total dose (mGy)	$\Delta\theta$ (deg)	N_{proj}	Exposure (mR)	Total dose (mGy)
10	0.45	23	11.2	0.4	0.13	89	43.4	1.5
20	0.45	45	22.0	0.8	0.23	89	43.4	1.5
30	0.45	67	32.7	1.2	0.34	89	43.4	1.5
40	0.45	89	43.4	1.5	0.45	89	43.4	1.5
50	0.45	111	54.2	1.9	0.56	89	43.4	1.5
70	0.45	157	76.6	2.7	0.79	89	43.4	1.5
90	0.45	201	98.1	3.5	1.01	89	43.4	1.5
120	0.45	267	130.3	4.6	1.35	89	43.4	1.5
150	0.45	333	162.6	5.8	1.69	89	43.4	1.5
180	0.45	401	195.7	6.9	2.03	89	43.4	1.5
200	0.45	445	217.2	7.7	2.25	89	43.4	1.5
240	0.45	533	260.2	9.2	2.70	89	43.4	1.5
280	0.45	623	304.1	10.8	3.15	89	43.4	1.5
320	0.45	711	347.1	12.3	3.60	89	43.4	1.5
360	0.45	800	390.5	13.8	4.05	89	43.4	1.5

number of projections used for each reconstruction varies linearly with θ_{tot}; and (2) constant number of projections (subsequently referred to as "constant-N_{proj}," with $N_{proj}=89$), in which case the angular separation between projections varies linearly with angle. The experimental conditions are summarized in Table I. The constant-$\Delta\theta$ scheme ensures that view sampling effects are constant for all settings of θ_{tot}, although total dose increases with θ_{tot} (such that quantum and electronic noise contributions vary. The constant N_{proj} scheme, on the other hand, imparts the same total dose for all settings of θ_{tot} (although view sampling effects vary), illustrating the scenario in which total dose represents a clinical constraint, and the system designer is considering the questions how large an orbital extent (θ_{tot}) and how many projections (N_{proj})?

Images were reconstructed at isotropic 0.518 mm voxel size, with a $(357\times357\times222)$ voxel volume occupying the interior of the clutter phantom. The voxel size was chosen to adequately resolve the smallest spheres in the phantom while maintaining a reasonable size for all the image data. A Hann apodization filter was used throughout, and no additional filters (e.g., interslice tomosynthesis filter in the f_y direction) were applied. Modified Parker weights[31,32] were adopted for reconstructions exceeding 180°+fan. For $\theta_{tot}=360°$, a uniform weighting of 0.5 was employed. The usual normalization factor π/N_{proj} applied for a 180°+fan acquisition[33] was modified for limited arc acquisition as θ_{tot}/N_{proj}, such that the Fourier coefficients within the sampled region were correctly normalized to be independent of N_{proj} and the reconstructed voxel values were roughly proportional to θ_{tot}.

II.C. Measurements of signal, noise, and power spectral density

II.C.1. Signal difference to noise ratio (SDNR)

As a simple, intuitive means of assessing imaging performance under conditions of varying background clutter, the SDNR was measured using nylon cylinders in a polystyrene plate inserted at the central "coronal" plane of the clutter phantom as shown in Fig. 1(c). Analysis of SDNR was preliminary to S_B measurements (below) and was intended to: (1) Assess the validity of voxel values reconstructed as a function of θ_{tot} (i.e., proper signal normalization in reconstructed volumes as discussed in Sec. II B); (2) qualitatively illustrate the influence of θ_{tot} and background noise on the visibility of stimuli; and (3) give basic quantitation by way of a simple metric invoked in other studies and sometimes related to the Rose criterion for detectability. The coronal plate consisted of a 1 cm slab of polystyrene embedded with an assortment of nylon cylinders [1 cm height and diameter; Fig. 1(c)]. The nylon cylinders presented "stimuli" within the coronal plane amid varying degrees of anatomical clutter under different acquisition angles. For $\theta_{tot}=360°$, the coronal plane presents stimuli within a uniform (polystyrene) background, while for $\theta_{tot}<180°$+fan, out-of-plane clutter arising from the adjacent volumes of random spheres increases with smaller tomosynthesis arc. The SDNR was analyzed as

$$\mathrm{SDNR}=\frac{\mu_{\mathrm{Stimulus}}-\mu_{\mathrm{Background}}}{\sigma_{\mathrm{Background}}}, \tag{6}$$

where μ_{Stimulus} and $\mu_{\mathrm{Background}}$ denote the mean voxel value within the region of the stimulus and background ROIs, respectively, as illustrated in Fig. 2, and $\sigma_{\mathrm{Background}}$ is the stan-

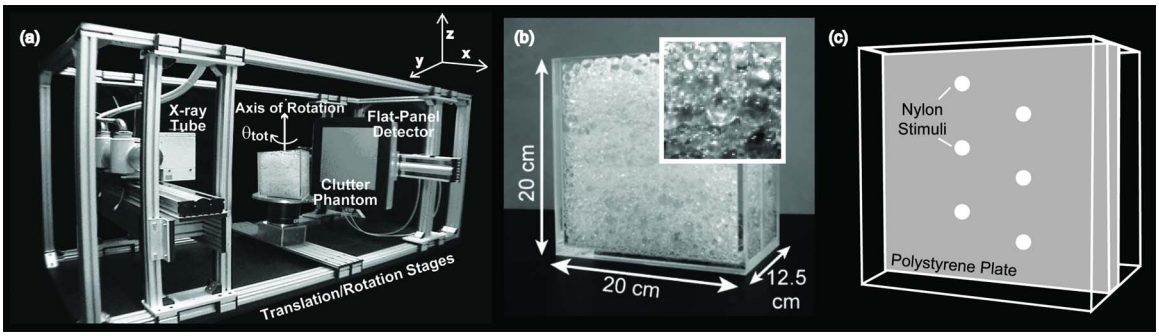

FIG. 1. Experimental setup. (a) The imaging bench showing basic components and coordinates for tomosynthesis and CBCT. (b) The clutter phantom was based on properties of fractal self-similarity, by which equal volumes of differently sized spheres were found to give a power-law exponent β_{obj} of approximately 3. (c) A polystyrene plate inserted into the clutter phantom was embedded with nylon cylinders used for SDNR measurements. Clutter power spectrum measurements used only the random set of spheres (polystyrene plate removed).

dard deviation in voxel values belonging to the background ROIs (chosen large enough that the standard deviation reflects the out-of-plane "anatomical noise"). Measurements were performed about each stimulus, with SDNR averaged over six stimuli and across 13 coronal slices within the polystyrene slab.

II.C.2. Measurement of background power spectra

II.C.2.a. 3D background power spectra. The background power spectrum associated with clutter presented by the phantom of Fig. 1(b) was measured as a function of θ_{tot} for both the constant-$\Delta\theta$ and constant-N_{proj} cases. Nonoverlapping volumes of interest (VOIs), each $50\times50\times50$ pixels ($25.9\times25.9\times25.9$ mm^3), were selected within the reconstructed volume (total number of VOIs=144). The size of the VOIs was sufficiently large to encompass structures of interest (different diameter of spheres) but small enough to avoid long-range shading artifacts. The background power spectrum was given by the square of the magnitude of the discrete Fourier transform of each VOI, with the ensemble mean subtracted

$$S_B(f_x,f_y,f_z)=\frac{\Delta_x\Delta_y\Delta_z}{N_xN_yN_z}\frac{1}{\mathrm{Norm}_W}\langle|FT[W(x,y,z)\cdot(\mathrm{VOI}(x,y,z)-\overline{\mathrm{VOI}})]|^2\rangle, \quad (7a)$$

where Δ_i and N_i are the voxel size and extent of each VOI in the ith direction, respectively. S_B written as such is the abso-

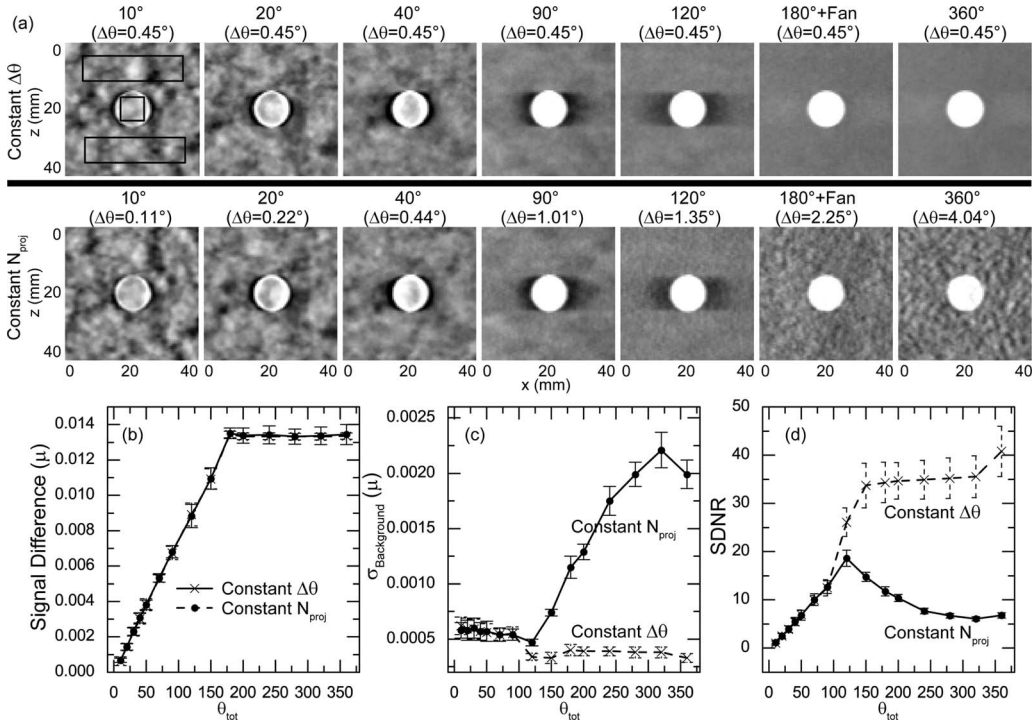

FIG. 2. Coronal images of the clutter phantom including a conspicuous stimulus (nylon cylinder) for illustration of clutter rejection and measurement of SDNR. (a) Images acquired as a function of θ_{tot}. Regions of interest for calculation of stimulus and background mean and standard deviation are shown as black rectangles in the first image. (b) Signal difference, (c) background noise ($\sigma_{Background}$), and (d) SDNR plotted as a function of angular extent.

lute power spectrum, and has units of μ^2 mm^3, where μ denotes the units of reconstructed voxel values and is written explicitly without cancellation of terms to clearly convey units of signal$^2\times$length^3. For $\theta_{\text{tot}}>180°$+fan (i.e., CBCT), the units of μ are mm^{-1} corresponding to attenuation coefficient, while for limited arcs (i.e., tomosynthesis), the voxel value is expected to depend on the orbital extent, and μ is interpreted simply as the units of the voxel value "signal."

To compare the background clutter power relative to signal power, the absolute power spectrum was divided by the square of the signal mean to yield normalized power spectrum

$$S_B(f_x,f_y,f_z)=\frac{1}{\overline{\text{VOI}}^2}\frac{\Delta_x\Delta_y\Delta_z}{N_xN_yN_z}\frac{1}{\text{Norm}_W}\langle|FT[W(x,y,z)\cdot(\text{VOI}(x,y,z)-\overline{\text{VOI}})]|^2\rangle, \quad (7b)$$

where $\overline{\text{VOI}}$ denotes the ensemble mean voxel value. This form normalizes the effect of increasing signal power with orbital extent and facilitates the comparison of clutter power. Thus, normalized power spectra are presented below and used in power-law parameter fitting in Sec. III C, with units of mm^3. The term $W(x,y,z)$ is a 3D Hann tapering window applied to individual VOIs to reduce spectral leakage

$$W(r)=\begin{cases}1/2[1+\cos(\pi r/R)] & \text{for } r\le R\\ 0 & \text{otherwise}\end{cases}, \quad (8)$$

where $r=\sqrt{x^2+y^2+z^2}$ and R is half the width of the VOI. The normalization factor

$$\text{Norm}_W=\frac{\sum_i|W_i|^2}{n} \quad (9)$$

restores the proper magnitude of the power spectrum following the tapering window, with W_i denoting the elements of the matrix $W(x,y,z)$ and n the number of elements in the matrix. While a tapering window is often unnecessary in analysis of the quantum noise-power spectrum, we found it useful in reducing spectral leakage associated with the sharply decreasing $(1/f)$ characteristic of the background power spectrum. The statistical error in the power spectrum (denoted by error bars in plots below) was calculated as the standard deviation across the ensemble at each spatial frequency, divided by the square root of the number of VOIs in the measurement.

To analyze the component of the power spectrum owing to quantum noise and electronic noise, two repeated scans were acquired (with the clutter phantom in exactly the same position between scans) and the two reconstructed volumes were subtracted. The resulting 3D difference image presents stochastic noise components (quantum and electronic noise, amplified by $\sqrt{2}$) contributing independently between the two scans. Assuming the frequency characteristics of stochastic noise components remain unchanged between consecutive scans, the power spectrum of the difference image captures fluctuations due to quantum and electronic noise. To reduce the influence of quantum and electronic noise on the anatomical background power spectrum measurement, the difference between the power spectrum of the 3D clutter volume and that of the subtracted volume (divided by 2) was taken as the power spectrum of anatomical clutter alone, i.e., $S_B=S_{I_1}-S_{I_1-I_2}/2$.

II.C.2.b. 2D "slice" power spectra. Two-dimensional slice power spectra were computed in a similar way as the 3D power spectra described above. Nonoverlapping ROIs of 50×50 voxels (25.9×25.9 mm^2) were drawn from coronal (x,z) slices of reconstructed volumes (total number of ROIs=7632). A 2D Hann window and normalization factor was applied, and the 2D Fourier transform was computed, scaled by $\Delta_x\Delta_z/N_xN_z$. The slice power spectrum determined in this way (i.e., slice "extraction") corresponds to the integral of the 3D power spectrum along the depth (f_y) direction as described by Siewerdsen *et al.*[34] This point bears reiteration: the 2D power spectrum of an image slice "extracted" from a 3D image is *not* a slice from the 3D power spectrum; it is the integral over the 3D power spectrum in the orthogonal direction. The units of the 2D slice power spectrum and 3D power spectrum differ by a factor of length. The relevance of slice or "volumetric" power spectra pertain to the expected value of β and also to the observer model being considered, as discussed below, e.g., whether the observer is considered to have information belonging only to a slice or is able to completely interrogate the volume.

II.C.3. Power-law noise parameters (κ and β)

As a basic empirical characterization of the measured power spectra in terms that can be compared to previous work, the measurements were fit to the power-law description of Eq. (1). The region of the power spectrum expected to follow a power-law characteristic is bounded by the reciprocal of the largest and smallest diameters of the spheres in the phantom. For the phantom of Fig. 1(b), this gave a spatial frequency range between $(1/15.88=0.063$ mm$^{-1})$ and $(1/3.18=0.33$ mm$^{-1})$.

The dependence of the power-law parameters κ and β on the tomosynthesis angle (θ_{tot}) was characterized in order to examine the behavior of out-of-plane clutter in the continuum from a projection image to a fully 3D reconstruction. Asymmetries in κ and β in the f_x, f_y, and f_z directions were also examined. As described in Appendix A, analysis of the clutter power spectrum predicts distinct behavior in κ and β in each regard (i.e., as a function of θ_{tot} and asymmetric in x, y, and z), showing also that the pure power-law form breaks down in tomosynthesis (although the power spectrum could still be fit to such an empirical form). To simplify the analysis, a 1D representation of the 3D power spectrum was obtained by extracting 1D profiles along the f_x, f_y, and f_z axes, giving $S_B(f_x)$, $S_B(f_y)$, and $S_B(f_z)$. Linear regression with the least squares approach was performed on the log-log data points to obtain the power-law parameters κ and β

$$\log(S_B)=\log(\kappa)-\beta\log(f). \quad (10)$$

Parameters corresponding to $S_B(f_x)$, $S_B(f_y)$, and $S_B(f_z)$ were denoted as κ_x, κ_y, κ_z and β_x, β_y, β_z. The negative of the slope

of the regression line gives β, while the intercept equals $\log(\kappa)$. Note that one could alternatively write $\log(S_{B-\mathrm{obj}}) = \log(\kappa_{\mathrm{obj}}) - \beta_{\mathrm{obj}} \log(f)$, and that one could infer $S_{B-\mathrm{obj}}$ from the measured S_B by dividing MTF^2. At low spatial frequencies (where anatomical clutter predominates), division by MTF^2 effects a small correction; at high frequencies, on the other hand, we found the correction to perturb the power spectra tails and yield poor fits. Thus, where explicitly mentioned below, the assumption $\kappa = \kappa_{\mathrm{obj}}$ and $\beta = \beta_{\mathrm{obj}}$ may be invoked, believed to be a fair approximation, since the fits were from the low-frequency regime. In fact, the main aim of the work is not a precise determination of κ_{obj} and β_{obj} but an investigation of their effect on d', the sensitivity of which was examined across broad variations of these power-law parameters.

Error bars on β and κ were computed using the *regstats* function in MATLAB (vR2007a, The Mathworks, Natick, MA) to reflect standard errors of the slope and intercept associated with the least squares fit,[35] with the standard error of the intercept obtained from linear regression corresponding to $\log(\kappa)$. Assuming the error is small, propagation of errors gives the standard error in κ as $\kappa \times \Delta[\log(\kappa)]$, where $\Delta[\log(\kappa)]$ denotes the standard error of $\log(\kappa)$. Errors computed as such reflect the standard deviation of the distribution of the "true" β and $\log(\kappa)$.

II.D. Detectability index in tomosynthesis and CBCT

As described previously, cascaded system analysis (CSA) can be used to model the NPS and noise-equivalent quanta (NEQ) of tomosynthesis and CBCT.[24,25,36] Such analysis models the imaging chain as a serial (and/or parallel[37]) cascade of stages that govern the propagation of spatial-frequency-dependent signal and noise. Previous analysis demonstrated agreement of theoretical and experimental 3D NPS and NEQ, illustrated the effect of various acquisition and reconstruction parameters on the NEQ, and analyzed task-based performance in terms of the detectability index[38]

$$d'^2 = \int\int\int \frac{\mathrm{MTF}^2(f_x,f_y,f_z)}{S_Q(f_x,f_y,f_z) + S_E(f_x,f_y,f_z)} \cdot |\Delta H(f_x,f_y,f_z)|^2 df_x df_y df_z, \tag{11a}$$

where MTF is the modulation transfer function of the system, ΔH is the task function (modeled as the Fourier transform of the difference in two hypotheses, e.g., signal-present versus signal-absent in detection tasks), and S_Q and S_E denote the 3D quantum and electronic NPS, respectively. The 3D CSA model for S_Q and S_E as derived previously yields[25,39,40]

$$S_Q = \left(\frac{\theta_{\mathrm{tot}}}{\bar{q}_0}\right) \frac{1}{mM^2(a_{\mathrm{pd}}^2 \bar{g}_1 \bar{g}_2 \bar{g}_4)^2} \cdot \left[(a_{\mathrm{pd}}^4 \bar{g}_1 \bar{g}_2 \bar{g}_4 (1 + \bar{g}_4 P_K T_3^2) T_5^2 * * III_6 T_8^2) * * III_8 T_{11}^2 T_{12}^2 \cdot \frac{\widetilde{f^2}}{f} * * * III_{15} \right] T_{15}^2 * * * III_{15}, \tag{11b}$$

$$S_E = \left(\frac{\theta_{\mathrm{tot}}}{\bar{q}_0^2}\right) \frac{1}{mM^2(a_{\mathrm{pd}}^2 \bar{g}_1 \bar{g}_2 \bar{g}_4)^2} \cdot \left[(S_{\mathrm{add}} T_8^2) * * III_8 T_{11}^2 T_{12}^2 \frac{\widetilde{f^2}}{f} * * * III_{15} \right] \cdot T_{15}^2 * * * III_{15}, \tag{11c}$$

where notation is consistent with previous work. The terms $\overline{q_0}$ denotes the mean incident x-ray fluence, θ_{tot} refers to the orbital extent, a_{pd} describes width of photodiode, and P_K is the transfer function associated with K-fluorescence as described by Yao[37] and Richard.[18] The 2D power spectrum of electronics noise is represented by S_{add}, and includes the effects of pixel dark noise, amplifier noise, etc.[39,40] Gain factors associated with gain stages are denoted as $\bar{g}_i$, and the transfer function for spatial spreading (stochastic blur or aperture integration) at stage i is written as T_i. The exact forms of the gain factors and transfer functions, as well as the physical process represented by each stage, are described in detail in Refs. 25, 39, and 40.

Such analysis is useful in understanding the fairly complex interplay between various factors in the 2D projection cascade (e.g., scintillator or photoconductor MTF, pixel pitch, and electronic noise) and the 3D reconstruction cascade (e.g., choice of apodization filters and 3D sampling). While the model describes the NEQ and detectability index in a continuum of θ_{tot} (ranging from a single projection to tomosynthesis and CBCT), previous works have not included the effect of background anatomical noise on detectability. While the background power spectrum does not represent a truly stochastic process, a simple approach proposed by Barrett *et al.*[41] includes S_B as an additional term in the denominator of the NEQ, referred to as a generalized NEQ. This suggests a generalized detectability index as follows:

$$d'^2 = \int\int\int \frac{\mathrm{MTF}^2(f_x,f_y,f_z)}{S_B(f_x,f_y,f_z) + S_Q(f_x,f_y,f_z) + S_E(f_x,f_y,f_z)} \cdot |\Delta H(f_x,f_y,f_z)|^2 df_x df_y df_z. \tag{11d}$$

Note that S_B, S_E, and S_Q used in detectability calculation are absolute power spectra with units μ^2 mm^3. This form allows analysis of the tradeoffs between S_B, S_Q, and S_E with respect to, for example, θ_{tot}, the exposure per projection, and the total number of projections. Under conditions of constant total dose and constant angular separation, increasing θ_{tot} reduces S_B (i.e., rejects out-of-plane clutter, as shown below) but increases S_Q and the relative contribution of S_E (due to a lower dose per projection). Similarly, spreading fewer, higher dose projections over a larger angular range may reduce the effect of S_E but at the cost of view-sampling effects that impede detectability. Tradeoffs among quantum noise, electronic noise, and out-of-plane clutter are immediately apparent that are central to knowledgeable system design, e.g., in breast and chest tomosynthesis, and their interdependency as in Eq. (11d) shows that they cannot be considered in isolation from other aspects of system performance.

The dependence of d' on θ_{tot} and other parameters was analyzed as a function of: (i) Power-law characteristics of clutter (κ_{obj} and β_{obj}); (ii) the number of projections; and (iii) total dose. In the first case, power-law parameters were taken from experimental measurements of κ and β for the phantom described previously, noting the assumption above for conditions in which $\kappa \approx \kappa_{obj}$ and $\beta \approx \beta_{obj}$. We also allowed κ_{obj} and β_{obj} to vary freely across wide ranges of values [$\beta_{obj}=2-4$, $\kappa_{obj}=(10^{-5}\sim 10^{2})\times\kappa_{measured}$ (μ^2 mm^3)] to examine sensitivity to each. In each case, the same system geometry, beam quality, etc. as described above were assumed, with attenuation by a 10 cm slab of water taken as an approximation to the phantom. A constant exposure to the detector from view to view was assumed. Detectability index was calculated based on Eq. (11d) in a manner that accounted for the angular separation between projections (view sampling), as detailed in Appendix B.

Three idealized imaging tasks were modeled to illustrate the dependence of performance on acquisition parameters such as θ_{tot}, N_{proj}, and dose: (i) A nominal 3 mm sphere detection task, which emphasizes low and middle frequencies, with the contrast of the sphere set to that measured for the nylon stimulus in the SDNR phantom (0.12 mm^{-1} in the 360° CBCT images); (ii) a delta-function detection task implemented as a constant at all spatial frequencies, and (iii) a Gaussian with a width (standard deviation) of 3 mm, representing a low-frequency task. The latter two tasks carried equal signal power [i.e., integral over $H^2(f_x,f_y,f_z)$] as task (i) to emphasize frequency-dependent characteristics rather than signal magnitude.

III. RESULTS

III.A. SDNR

Example coronal images acquired as a function of θ_{tot} in both the constant-$\Delta\theta$ and constant-N_{proj} schemes are shown in Fig. 2(a). The images show the stimulus (nylon cylinders) and the ROIs used for characterization of SDNR. The ROIs were placed to represent the mean and standard deviation in the stimulus and background while avoiding the dark edge bands (edge enhancement effect of the ramp filter along the x direction) that are conspicuous at low θ_{tot}. Out-of-plane clutter evident at small tomosynthesis arc is gradually rejected as orbital extent increases. At large orbital extent ($\theta_{tot}=180°$ +fan to 360°), out-of-plane clutter is completely rejected, and distinct tradeoffs in quantum noise, electronic noise, and view aliasing are observed. For the constant-$\Delta\theta$ case, a smooth quantum noise background is evident. For the constant-N_{proj} cases, view aliasing effects as a result of large angular separation between projections can be observed as streaks in the axial plane and granular mottle in the coronal plane.

Signal difference, background noise, and SDNR are shown as a function of θ_{tot} for both acquisition schemes in Figs. 2(b)–2(d). For both cases, the signal difference increases linearly as a function of θ_{tot} up to 180°+fan, beyond which it is a constant given by the true difference in attenuation coefficients ($\mu_{nylon}-\mu_{polystyrene}$). This behavior is consistent with expectations for properly normalized projections backprojected across a limited arc, i.e., voxel value proportional to the tomosynthesis arc and independent of N_{proj}. The constant voxel value above $\theta_{tot}=180°$+fan confirms proper Parker weighting.[32,42]

For the constant-$\Delta\theta$ case, background noise decreases with θ_{tot} as out-of-plane clutter is gradually rejected, giving a monotonic increase in SDNR with angle. For the constant N_{proj} case, background noise decreases with θ_{tot} up to a point (determined by the system geometry and choice of N_{proj}) beyond which view aliasing begins to dominate. For the conditions described above ($N_{proj}=89$, SAD=93.5 cm, and SDD=144.4 cm), background noise increases sharply due to view aliasing beyond $\theta_{tot}\sim 120°$. This effect is also reflected in the SDNR measurements for the constant N_{proj} case, where SDNR improves up to $\theta_{tot}\sim 120°$, beyond which SDNR declines even after the object is fully sampled (180°+fan), reflecting increasing severity of view aliasing artifacts as $\Delta\theta$ increases.

III.B. Background power spectra

Coronal (x,z) and axial (x,y) slices of the clutter phantom reconstructed under the constant-$\Delta\theta$ and constant-N_{proj} schemes are shown in Fig. 3. Window and level of each image were set to its mean ±3 standard deviations for display and intercomparison. In the coronal plane, the overall impression of contrast and noise as a function of θ_{tot} is consistent with that observed in the SDNR measurements (Fig. 2), with background clutter dominating at low θ_{tot} and view aliasing dominating at large θ_{tot} (for constant-N_{proj}). As expected in the axial plane, depth resolution along the y direction improves with θ_{tot}.

Figure 4 shows the coronal and axial normalized power spectra corresponding to the images of Fig. 3. The frequency domain plotted ranges $\pm f_{Nyquist}$ in the f_x, f_y, and f_z directions. The logarithmic grayscale helps to visualize the broad range in spectral density, dominated by the large low-frequency component of long-range "anatomical" clutter. The overall magnitude of the normalized power spectra decreases with θ_{tot}. The coronal power spectra exhibit the "missing cone" artifact about the f_z axis associated with circular cone-beam CT, the extent of which is consistent with the system geometry.[43] The most notable feature of the power spectra is the "double-wedge" of spectral density about the f_x direction of the axial power spectra. The double-wedge widens with (and is equal to) θ_{tot} as expected and corresponds to the sampled region of the Fourier domain according to the central slice theorem.

Power spectra along f_x and f_z axes were extracted from the 3D power spectrum measurements for constant-$\Delta\theta$ and constant-N_{proj}, as summarized in Fig. 5. Spectra along f_y are not shown for reasons of brevity and because the spectral density is extremely low (near zero, within the unsampled region of the double-wedge) for $\theta_{tot}<180°$+fan. The vertical dashed lines mark the frequency range over which the power spectra are expected to obey power-law behavior (i.e., the reciprocal of the largest and smallest diameter spheres, 0.063

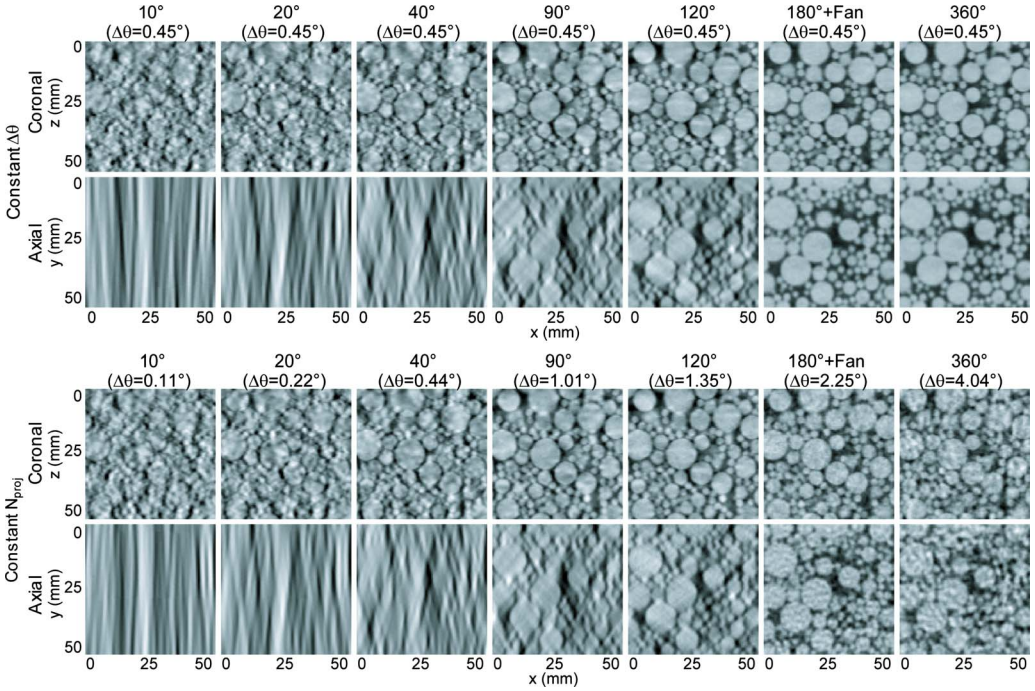

FIG. 3. Coronal and axial slices of the clutter phantom in tomosynthesis and CBCT. Rejection of out-of-plane clutter and spatial resolution along y each improve with orbital extent. View aliasing artifacts are evident in images reconstructed with large angular separation (e.g., the constant-N_{proj} scheme at large θ_{tot}).

and 0.31 mm^{-1}). The log-log plots over this region demonstrate fairly good linearity ($R^2=0.96\pm0.02$), consistent with a power-law form proportional to $1/f$. Below this region, the power spectrum measurements are subject to longer range fluctuations, such as shading artifacts not corrected by detrending. Above this region, a sharp decline in the power spectra is evident, associated with correlation on scales finer than the smallest sphere in the phantom (e.g., scintillator MTF and reconstruction filter). Near the Nyquist frequency, the tails of the power spectra tend to flatten due to the presence of (white) electronic noise and aliasing.

From the power-law (linear) region of each plot, the mag-

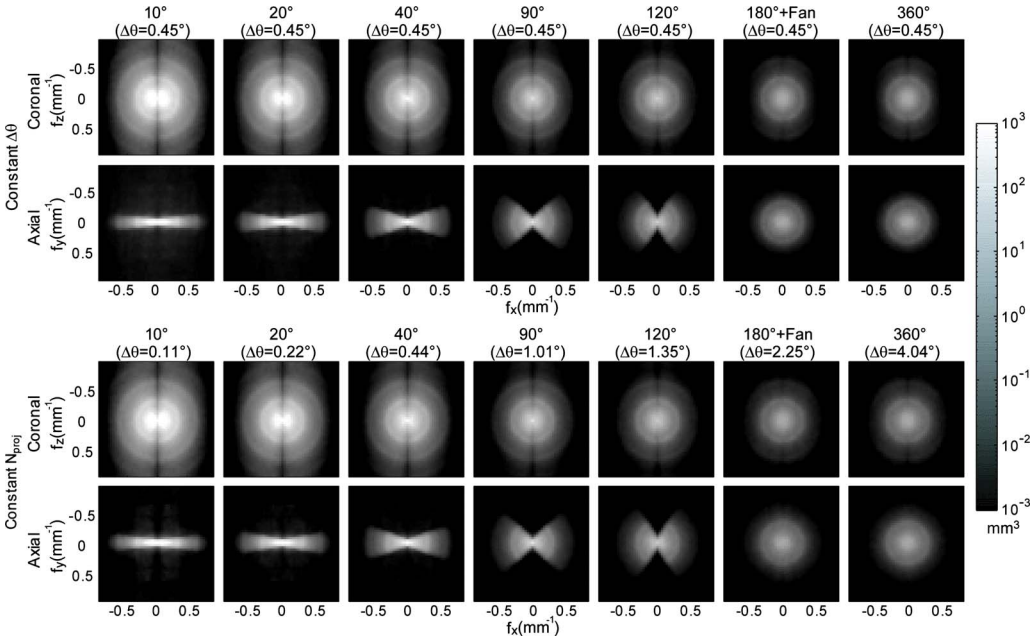

FIG. 4. Coronal and axial slices of the normalized 3D power spectra of clutter phantom images. The frequency domain ranges $\pm f_{\text{Nyquist}}$ in the f_x, f_y, and f_z directions. The large low-frequency component of anatomical clutter is clearly observed, with overall magnitude decreasing with θ_{tot}. The double-wedge of spectral density in the axial slices corresponds to the sampled region in the Fourier space.

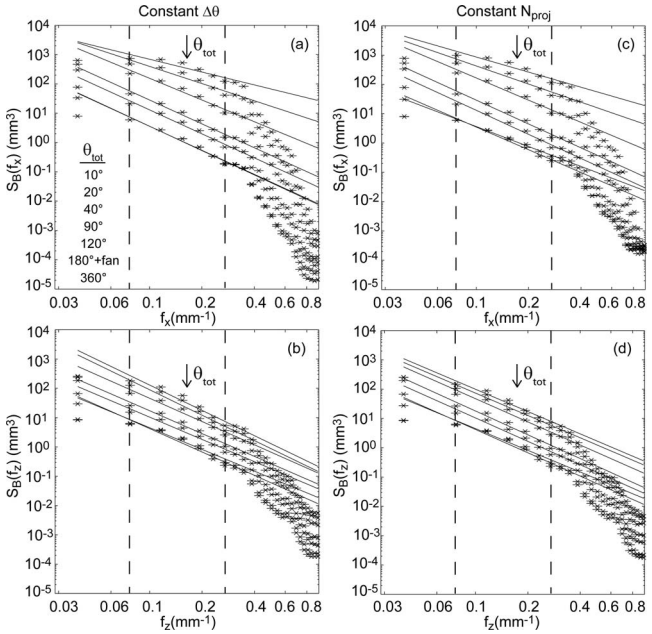

FIG. 5. Normalized power spectra measurements along f_x and f_z axes extracted from the 3D power spectrum measurements for the constant $\Delta\theta$ [(a), (b)] and constant N_{proj} [(c), (d)] schemes. Power spectra are shown for seven orbital extents ranging from 10° to 360° as in the legend. The vertical dashed lines mark the frequency range over which the power spectra are expected to obey power-law behavior (i.e., the reciprocal of the largest and smallest diameter spheres, 0.063 mm^{-1} and 0.31 mm^{-1}). Power spectra exhibit good linearity within this region ($R^2=0.96\pm0.02$), consistent with a power-law relationship. The magnitude of the power spectra is seen to decrease with increasing θ_{tot}, quantifying the gradual rejection of out-of-plane clutter for larger tomosynthesis angle.

nitude of the background power spectrum is seen to decrease with increasing θ_{tot}, quantifying the gradual rejection of out-of-plane clutter for larger tomosynthesis angle. Comparing $S_B(f_x)$ for the two reconstruction schemes, the constant N_{proj} case exhibits greater midfrequency and high-frequency noise components at large θ_{tot} associated with the view sampling effects described above.

III.C. Power-law parameters, β and κ

Figure 6 shows measurements of β and κ along f_x and f_z (denoted, respectively, as β_x, β_z and κ_x, κ_z) obtained from linear fits to the power spectra within the frequency range expected to follow power-law behavior. Each plot shows β and κ determined from the power spectrum of (i) a single projection (plotted at $\theta_{\text{tot}}=0°$); (ii) a 3D image reconstruction from tomosynthesis or CBCT; and (iii) a coronal slice extracted from the 3D image (recognizing that the slice power spectrum involves an intrinsic integration along f_y and a change in units in κ, as described above). As shown in Appendix A, a slice from tomosynthesis images of power-law clutter does not strictly exhibit a κ/f^{β} characteristic, except for special cases on the f_x and f_z axes. In light of this finding, the power-law parameters κ and β shown below should be considered a purely empirical description of the 2D slice power spectra.

The results for β_x and β_z are summarized in Figs. 6(a)–6(d), showing the following overall trends: β_x increases with θ_{tot} for tomosynthesis ($\theta_{\text{tot}}<\sim180°$); above $\theta_{\text{tot}}\sim180°$, β_x remains constant for the constant-$\Delta\theta$ case and reduces for the constant-N_{proj} case; and β_z is roughly constant with θ_{tot}. Since a larger value of β corresponds to increased low-frequency correlation (qualitatively appreciated as clumpiness), the increase in β with θ_{tot} may at first seem counterintuitive; however, as evident in the images of Fig. 3, the effect is consistent with out-of-plane clutter rejection and better discrimination of the cross section of spheres achieved in higher angle reconstructions. As noted below, the real power of increasing θ_{tot} is in the reduction in κ, rather than its effect on β.

For the constant-$\Delta\theta$ case [Fig. 6(a)], β_x increases with θ_{tot}, and plateaus beyond $\theta_{\text{tot}}\sim90°$ for the 3D case and $\sim180°$ for the slice case. As expected (see Appendix A), the value of β is the same (within experimental error) for a single projection and a fully sampled ($\theta_{\text{tot}}\geq180°$+fan) 3D reconstruction, which is in turn equal to the β characterizing power-law behavior of the object (β_{obj}), assuming MTF corrections at low frequencies are small as explained in Sec. II C 3. For very small tomosynthesis angles, β is nearly the same for the slice and "3D" cases: The slice power spectrum approaches that of a filtered projection, reducing β_x by approximately 1 from β_{obj}; similarly for 3D power spectra, the effect of the ramp filter is not canceled by the reconstruction filter ($1/f_{2D}$), thus also decreasing 3D β_x from β_{obj} by ~1. This difference is quickly recovered as θ_{tot} increases, although the slice and 3D cases approach separate values of β at large θ_{tot}, which are also expected to differ by 1.[15,22] A difference in β_x of approximately 0.7 is observed in this case, the discrepancy owing to the fact that slice power spectra integrate along the f_y direction over all frequencies, while the phantom only follows power-law behavior over a limited frequency range. For the constant-N_{proj} case [Fig. 6(c)], β_x exhibits similar behavior, except that the slice and 3D cases decrease for $\theta_{\text{tot}}>180°$ as view aliasing effects impart an increasing level of "graininess" in the images.

In comparison, β_z is nearly constant with θ_{tot} in both cases [Figs. 6(b) and 6(d)] for "projections," slices, and 3D with a notable exception above $\theta_{\text{tot}}=180°$+fan. According to the central slice theorem and as shown in Fig. 4, the 3D power spectra are empty along f_y below $\theta_{\text{tot}}=180°$+fan; therefore, integration of the along the f_y-direction is equivalent to "adding" the power spectra of different views, which would not affect the slope ("color") of the spectra. Therefore, β_z is equal for the projection, slice, and 3D cases before the double-wedge fills the Fourier domain. Above $\theta_{\text{tot}}=180°$+fan, a precipitous drop in β_z occurs for the slice power spectrum as the Fourier domain fills in about the f_y axis, giving a decrease in β_z of ~0.7 from the 3D case, less than the nominal value of 1, as noted above. The values of β_z is comparable to that of β_x above 180°+fan.

Figure 6 also summarizes measurements of κ, with a logarithmic scale better showing the strong dependence on θ_{tot}. Values of κ for 3D reconstructions and 2D slices through the

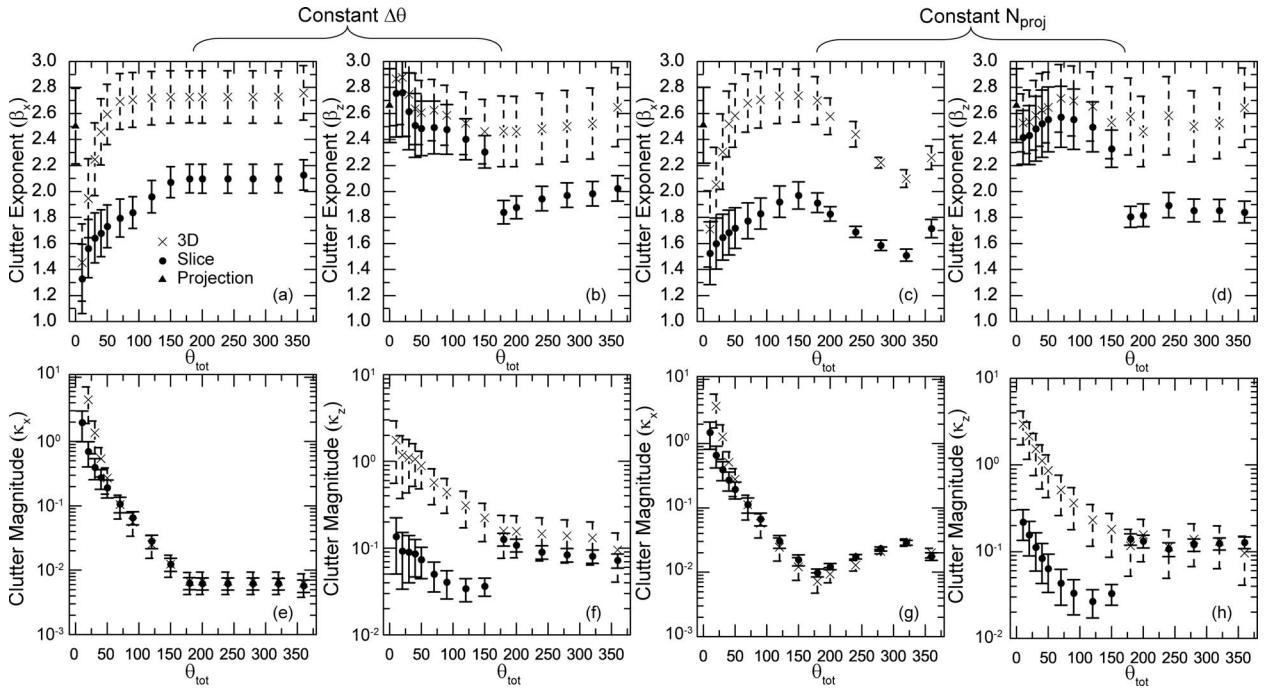

FIG. 6. Measurements of β and κ obtained from linear regression of the normalized power spectra in Fig. 5. The plots show β_x, β_z, κ_x, and κ_z determined under conditions of [(a), (b), (e) and (f)] constant-$\Delta\theta$ and [(c), (d), (g), and (h)] constant-N_{proj}. The units of κ for the 3D case are mm^3, while for projection and slice, the units are mm^2.

3D reconstruction are shown in the same graph despite the difference in units (κ for 3D reconstruction carries units of mm^3, whereas the units of κ in a slice is mm^2). The value of κ for a single projection is not shown because of the difference in scale resulting from normalization (in a single projection, $\kappa_x = 2.18\times10^{-6}$ μ^2 mm^2, $\kappa_z = 1.80\times10^{-6}$ μ^2 mm^2).

In all cases, for $\theta_{tot} < 180°$+fan, κ_x and κ_z decrease two to three orders of magnitude with θ_{tot}, corresponding to stronger rejection of out-of-plane clutter for larger tomosynthesis angles. For the constant-$\Delta\theta$ case, κ_x is constant above $\theta_{tot} = 180°$+fan (fully sampled 3D data without further rejection of out-of-plane clutter), whereas for the constant N_{proj} case, κ_x actually increases with θ_{tot} due to view aliasing noise. The values of κ along both the f_x and f_z axes is similar for slice and 3D power spectra for fully sampled CBCT images, consistent with the analysis in Appendix A, where the two values are shown to differ by a constant of order unity.

Trends in the z direction [Figs. 6(f) and 6(h)] are similar, although κ_z is typically one to two orders of magnitude smaller than κ_x, attributable to the missing cone of frequencies about the f_z axis intrinsic to backprojection on a circular source-detector orbit. The κ_z for slice NPS exhibits a discontinuity at $\theta_{tot} = 180°$+fan. The value of κ_z is ~10 times smaller for the slice power spectrum compared to the 3D power spectrum (for $\theta_{tot} < 180°$+fan, owing to unsampled frequencies about the f_y axis) and jumps to a value nearly the same as the 3D case beyond 180°.

Overall, such experimental analysis of κ and β confirms numerous theoretical expectations of power-law noise, highlights nontrivial asymmetries in (f_x, f_y, f_z), and quantifies the significant dependence of background clutter on θ_{tot}. First, the measurements demonstrate the overall approach regarding an experimental phantom designed to present power-law noise in a fairly general manner (without reference to a specific organ or body site). Second, the measurements highlight and quantify the differences in power-law parameters (κ and β) associated with a 2D projection, a 3D tomosynthesis image ($0 < \theta_{tot} < 180°$+fan), a 3D CBCT image ($\theta_{tot} \geq 180°$+fan), and slice versus 3D representations thereof. The value of β measured here (typically in the range 2.4–2.8) is similar to that reported for breast [e.g., β=2.7–3.0 (Refs. 15, 22, and 23)], but more importantly and as detailed below, the results pose important implications for measurement and modeling of detectability in tomosynthesis—Specifically, that κ (rather than the much-reported and scrutinized β) is the major factor governing detectability, and improved detectability in tomosynthesis and CBCT is primarily attributable to reduction in κ (rather than β).

III.D. Detectablity index

Detectability index was calculated as a function of θ_{tot}, β_{obj}, κ_{obj}, dose, and N_{proj} for various imaging tasks as summarized in Fig. 7. Unless otherwise mentioned, the nominal values are: $\beta_{obj} = 2.76$, $\kappa_{obj} = 3.72\times10^{-7}$ (μ^2 mm^3) as measured in the clutter phantom (β_x and κ_x in the constant-$\Delta\theta$ case); exposure per projection=0.01 mR after attenuation by 10 cm of water, and $N_{proj} = 89$.

Figure 7 illustrates the dependence of d' on (a) the frequency content (β_{obj}) and (b) the magnitude (κ_{obj}) of background clutter for four different angular extents (θ_{tot}=10°, 40°, 90°, 180°). Calculations were performed for a 3 mm

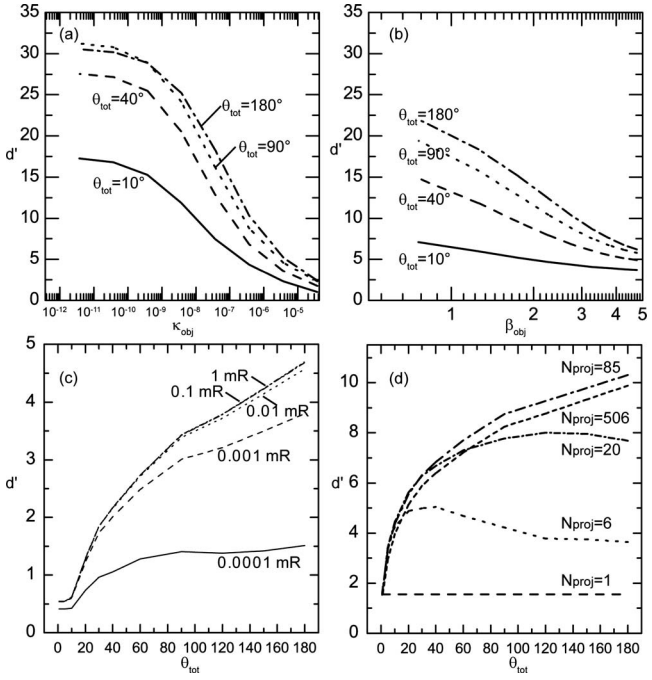

FIG. 7. Detectablity index (d') as a function of (a) κ_{obj} and (b) β_{obj}, for four orbital extents (sphere detection task). (c) Plot of d' versus θ_{tot} for different exposure levels (exposure to detector after attenuation by 10 cm of water), illustrating different levels of quantum noise relative to anatomical background noise (Gaussian detection task). (d) Plot of d' versus θ_{tot} for different total number of projections (N_{proj}), demonstrating effects of view aliasing at low N_{proj} (high θ_{tot}) and electronic noise at very high N_{proj} (sphere detection task).

sphere detection task. As expected, d' decreases with increasing clutter magnitude (κ_{obj}) and clumpiness (β_{obj}) at each θ_{tot}. Consistent with previous work,[44] a smaller value of β_{obj} gives improved detectability for all four settings of θ_{tot}. The same trend is observed with reduced clutter magnitude, but changes in κ_{obj} have a greater influence on detectability as seen by the large decrease in d' over an order magnitude decrease in κ_{obj} about the nominal value. In comparison, detectability is less sensitive to β_{obj} over the range examined, especially for low tomosynthesis angles (10° and 40°) and clinically relevant β_{obj} values (~2–4). Detectability generally increases with θ_{tot} around the nominal values of κ_{obj} and β_{obj}, illustrating the benefit of tomographic imaging in the presence of background clutter. However, at very small clutter magnitude ($\kappa_{obj}=3.72\times10^{-10}$, 3.72×10^{-11}, and 3.72×10^{-12} μ^2 mm^3), the cross-over between the 90° and 180° curves reflects the increasing contribution of quantum noise relative to anatomical clutter.

Figure 7(c) shows d' of a 3 mm Gaussian detection task versus θ_{tot} for different exposures (corresponding to different levels of quantum noise relative to anatomical clutter) ranging from 0.1 μR/projection to 1 mR/projection (exposure to the detector after attenuation by 10 cm of water). As expected, low exposure corresponds to a relatively high contribution of quantum noise, which dominates over anatomical clutter evidence by the nearly constant d' beyond $\theta_{tot}\sim80°$ in the 0.1 μR/projection curve. Increasing the exposure per projection reduces quantum noise and gives the expected monotonic increase in d' with θ_{tot}. However, further increase in exposure does not necessarily improve d', as the relative magnitude of quantum noise becomes small in comparison to anatomical noise, which is independent of dose. This last point illustrates the importance of the generalized NEQ and detectability index, whereas a conventional (quantum-noise-only) metric would suggest continuous performance improvement with dose. Through incorporation of background clutter in the generalized form, the point of diminishing returns can be identified, and a better understanding of dose dependence (both low-dose limits and high-dose diminishing returns) can be obtained.

The effect of N_{proj} on detectability is shown in Fig. 7(d), keeping the total exposure at 0.89 mR in each case. A 3 mm sphere detection task was used. The case $N_{proj}=1$ corresponds to d' for a (filtered) 2D projection, which is independent of θ_{tot}. For a small number of projections (e.g., $N_{proj}=6$) spreading over a large angle ($\theta_{tot}>40°$), view aliasing is the dominant noise source and reduces d' significantly. Such view aliasing effects are also present for $\theta_{tot}<40°$, but background clutter dominates, such that d' still improves with θ_{tot}. Such effects are evident qualitatively in the images of Fig. 3 and in the work of Zhao *et al.*,[45] who observed streaks in the power spectrum for angular separation ($\Delta\theta$) greater than 2°. For a greater number of projections (e.g., $N_{proj}=85$), angular separation between views is sufficiently fine that view aliasing effects are smaller, and d' improves monotonically with θ_{tot} due to rejection of out-of-plane clutter. For an even greater number of projections (e.g., $N_{proj}=506$), the exposure per projection is so low that electronic noise starts to reduce overall detectability. Such analysis serves as a quantitative guide to a fundamental system design question: for fixed total dose and angular range θ_{tot}, what is the optimal number of projections for a given imaging task?

III.E. Imaging performance optimization for specific imaging tasks

The univariate analysis in Fig. 7 is illustrated further in the surface plots of Fig. 8 for three imaging tasks: (a) Delta-function detection, (b) sphere detection, and (c) Gaussian detection. The delta-function task emphasizes all spatial frequencies equally and is therefore most affected by quantum and electronic noise (which dominate at high frequencies), evidenced by the rapid falloff of d' at large θ_{tot} for cases of large N_{proj} (where electronic noise dominates) and low N_{proj} (where quantum noise and view aliasing dominate). The "peak" of this surface identifies the optimal number of projections for a given angular range, in answer to the fundamental system design question mentioned above.

The sphere detection task emphasizes both low frequencies (associated with the sphere itself) as well as middle and high frequencies (associated with the edge of the sphere). For the low-frequency aspect of the task, pronounced improvement in d' is observed with increasing θ_{tot} due to rejection of out-of-plane clutter, but electronic noise is seen to diminish d' at large values of N_{proj} (i.e., very low exposure per projection). In comparison, the Gaussian detection task is pre-

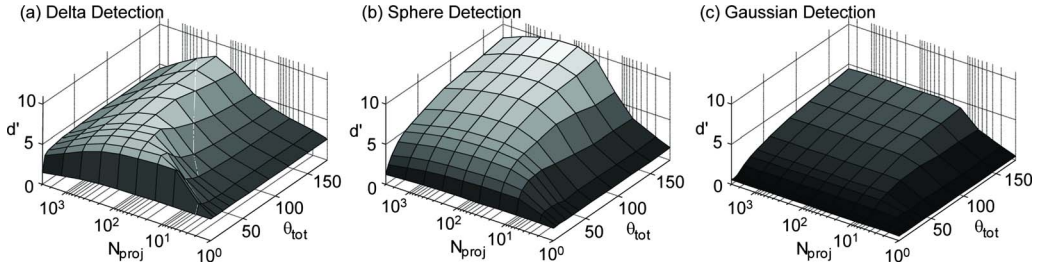

FIG. 8. Surface plots of d' versus N_{proj} and θ_{tot} for (a) delta-function detection task (uniform weighting of spatial frequencies), (b) a 3 mm sphere detection task (emphasizes low and middle frequencies), and (c) Gaussian detection task (a low-frequency task). Overall, lower-frequency tasks exhibit lower d' due to the influence of background clutter and benefit from increasing angular extent. Higher-frequency tasks are more susceptible to quantum and electronic noise, evidenced by falloff in d' for few projections over a large arc (small N_{proj} and large θ_{tot} with correspondingly high quantum noise and view aliasing) and large N_{proj} (low dose per projection with correspondingly high electronic noise).

dominantly a low-frequency task and is largely unaffected by high-frequency noise. Such a task is almost entirely "clutter-limited," and d' increases monotonically with angular extent. The effect of view aliasing is still evident for few projections spanning a large angle. Note also the overall decrease in d' for lower-frequency tasks, illustrating the impact of low-frequency background clutter and the importance of its inclusion in the generalized NEQ and detectability.

IV. DISCUSSION AND CONCLUSIONS

This work extends previous analytical modeling of the 3D noise-power spectrum, NEQ, and task-based detectability index for CBCT and tomosynthesis to include the effect of background clutter, measured and modeled according to a power-law characteristic and examined as a function of orbital extent, number of projections, and total dose.

Two simple imaging schemes were investigated, constant-$\Delta\theta$ and constant-N_{proj}, to represent varying degrees of quantum, electronic noise, and view aliasing artifacts on image quality, intending to conserve one noise source across angles while allowing others to vary. An alternative scheme (not studied directly in the current work) could involve constant-$\Delta\theta$ and constant total dose (with varying N_{proj}, dose per projection, and total orbital extent), which would also be of considerable value to the understanding of image quality in tomosynthesis at constant dose. In such a case, view aliasing and quantum noise are unchanged despite variation in orbital extent, while electronic noise increases with angle. Other schemes have also been proposed that involve uneven angular sampling and/or uneven distribution of dose across projections.[46] Investigation of such cases are subjects of future work.

A physical phantom was designed with acrylic spheres of different sizes to simulate a background exhibiting a power-law characteristic. Other authors have used similar designs. Sain *et al.*[47] used water filled plastic eggs submerged in radioactive water to simulate normal fatty tissue in the breast. Hestermann *et al.*[48] used a similar design with ellipsoid polystyrene beads as random, textured background to investigate system performance. Signal-to-noise ratio measured from the bead background and that from a simulated lumpy background were found to exhibit similar behavior except for a flattening at long exposure times. Park *et al.*[49] extended the design by using spheres of different sizes and densities. A similar computer-generated phantom was adopted by Badal *et al.*[50] to assess geometric accuracy in Monte Carlo simulation. The work presented above provides an analytical basis that explains the power-law nature of the sphere phantom design. The experimental phantom based on fractal self-similarity was found experimentally to give power-law spectral density that may be physically "tuned" to give κ_{obj} and β_{obj} analogous to that of anatomical structures such as the lung and breast. The work above did not attempt to model a particular anatomical site, investigating instead the effect of background clutter in general upon task-based performance. While appealing from a general standpoint and consistent with κ/f^{β} descriptions of anatomical noise, the phantom does not, of course, present the complexity of real anatomical structure, for example, asymmetries associated with ducts and vessels. The phantom design was based on fractal self-similarity, which predicts a β_{obj} of 3 in an object consisting of equal volume of differently sized spheres. A β_x value of 2.74 is observed in a fully 3D reconstruction, differing from the theoretical prediction of 3 because the phantom only obeys self-similarity over finite scales. The inclusion of system MTF in the measurement may also have contributed to the discrepancy.

The generalized performance metrics aim to include the effect of background clutter on image quality, extending previous work describing 3D quantum and electronic noise. Such is found to have significant influence on task-based detectability, especially (and to no surprise) for tasks involving low spatial frequencies (e.g., Gaussian detection). A generalized model also allows investigation of tradeoffs among each noise source with selection of θ_{tot}, N_{proj}, and dose. While the approach includes the effect of a finite number of views over a given orbital extent (i.e., "view aliasing"), other sources of image degradation, such as reconstruction artifacts (shading, streaks, etc.) are not included in the model, and the results assume that such artifacts can be ameliorated by acquisition and/or postprocessing techniques, e.g., a bowtie filter, scatter correction, etc.

The model for detectability index presented above [Eq. (11d)] corresponds to a very simple model observer (viz., a

prewhitening matched filter or Fisher–Hotelling model) and represents a fully 3D detectability index (i.e., a model in which the observer can take full advantage of the volumetric information). This is, of course, an idealized situation and may or may not correspond to an observer "scrolling" slices. Alternatively, the detectability within a single slice can be analyzed as the integral of the 3D signal over the 3D noise

$$d'^{2}_{\text{slice}} = \int\int \frac{[\int \text{MTF}(f_x,f_y,f_z)|\Delta H(f_x,f_y,f_z)|df_y]^2}{\int S_B(f_x,f_y,f_z) + S_Q(f_x,f_y,f_z) + S_E(f_x,f_y,f_z)df_y} df_x df_z. \quad (12)$$

Slightly more sophisticated observer models, such as nonprewhitening and eye filter models, can be incorporated within the same framework as described previously.[29] The correspondence of the theoretical detectability index (both d' and d'_{slice}) with real observers is the subject of future work.

As apparent in Eq. (11d), tradeoffs among anatomical background, quantum, and electronic noise are important to knowledgeable system design. Results in Sec. III D investigated the univariate dependence of imaging performance on background clutter (κ_{obj}, β_{obj}), exposure, and number of projections. The relevance of these tradeoffs are evident in Sec. III E, where the dependence on task is also demonstrated. Detection of nodules or masses (analogous to the low-frequency sphere or Gaussian detection tasks) benefit from a large angular extent for the rejection of clutter; conversely, detection/discrimination of small, high contrast structures such as microcalcifications (analogous to the delta-function detection task), suggests optimal performance from a limited arc with a knowledgably selected number of projections to divide the total dose in a manner that minimizes quantum and electronic noise. Although imaging techniques and reconstruction parameters (e.g., kVp, mA s, voxel size, reconstruction filters, etc.) chosen for this study are not necessarily representative of a specific clinical application (e.g., breast CT), the power-law characterization of anatomical noise still holds over the specified range of spatial frequencies, and the theoretical model can be easily adapted to specific imaging systems. Investigation of other variables that can potentially influence detectability will be subjects of future work. The CSA model accommodates different system design parameters, anatomical background, and imaging tasks, providing a general framework that can provide potential utility in a wide range of imaging applications.

ACKNOWLEDGMENTS

The authors extend thanks to Dr. Angel Pineda (California State University Fullerton, Fullerton, CA) and Dr. Rebecca Fahrig (Stanford University, Palo Alto, CA) for collaboration on topics of detectability and tomosynthesis associated with this work. Valuable conversations with Dr. Norbert Pelc (Stanford University, Palo Alto, CA) and Dr. John Boone (University of California Davis, Davis, CA) on the CT noise-power spectrum are gratefully acknowledged. Thanks also to Dr. Arthur Burgess (Harvard Medical School, retired) for insightful conversations regarding analysis of power-law spectra. The authors are grateful to Dr. Jerry Prince, Dr. J. Webster Stayman, and Dr. Wojtek Zbiewski (Johns Hopkins University) for insightful discussions regarding this work. This work was supported by the National Institutes of Health Grant No. R01-CA-112163.

APPENDIX A: POWER-LAW NOISE IN PROJECTIONS, TOMOSYNTHESIS, AND CBCT

The magnitude and frequency content of anatomical clutter is understood to vary among projection images, tomosynthesis, and cone-beam CT, with the first and last representing limiting cases of a continuum. The dependence of power-law noise in the limiting cases (2D projections and 3D cone-beam CT) has been described analytically by Metheany *et al.*[22] and experimental characterization of such has been the subject of considerable work. In this Appendix, a brief analytical description of power-law noise is offered that agrees in the limiting cases with the results of Metheany *et al.*[22] and characterizes the power spectrum across the continuum of tomosynthesis in a manner that aids interpretation of the experimental results reported above and by other authors. The analysis also distinguishes the expected form of power-law spectra as assessed from fully 3D volumes as opposed to individual slices therein.

1. The clutter power spectrum in the 3D object and the 3D CBCT image

Consider an object of extent L in the x, y, and z directions, with attenuation coefficient expressed as a stationary random variable, $\mu_{\text{obj}}(x,y,z)$, characterizing power-law clutter and with deviation from the mean denoted $\tilde{\mu}_{\text{obj}}(x,y,z)$. The Fourier transform of these deviations is written as $\tilde{M}_{\text{obj}}(f_x,f_y,f_z)$, such that the power spectral density of the object is

$$S_{B-\text{obj}}(f_x,f_y,f_z) = \frac{|\tilde{M}_{\text{obj}}(f_x,f_y,f_z)|^2}{L^3} = \frac{\kappa_{\text{obj}}}{(af_{\text{3D}})^{\beta_{\text{obj}}}}, \quad (A1)$$

where $f_{\text{3D}} = \sqrt{f_x^2+f_y^2+f_z^2}$. The units of $S_{B-\text{obj}}$ and $\tilde{M}_{\text{obj}}$ are μ^2 mm^3 and μ mm^3, respectively, with μ and a consistent with definitions in Sec. II. For a perfect 3D reconstruction (fully sampled and free of artifacts), the Fourier domain image is equal to the Fourier transform of the object, i.e., $\tilde{M}^{\text{3D}}_{\text{CBCT}}(f_x,f_y,f_z) = \tilde{M}_{\text{obj}}(f_x,f_y,f_z)$. The power spectrum of the 3D image therefore equals that of the object, i.e., $S^{\text{3D}}_{\text{CBCT}}(f_x,f_y,f_z) = S_{B-\text{obj}}(f_x,f_y,f_z)$.

2. The clutter power spectrum in a 2D projection

A projection image corresponds to integration of $\mu(x,y,z)$ across one dimension of the 3D spatial domain, and according to the projection slice theorem, its Fourier transform, denoted $\tilde{M}_{\text{proj}}(f_x,f_z)$, is a slice of that of the object, i.e., $\tilde{M}_{\text{proj}}(f_x,f_z) = \tilde{M}_{\text{obj}}(f_x,0,f_z)$. The power spectrum of a projection is therefore

$$S^{2D}_{proj}(f_x,f_z) = \frac{|\tilde{M}_{proj}(f_x,f_z)|^2}{L^2} = \frac{|\tilde{M}_{obj}(f_x,0,f_z)|^2}{L^2}$$
$$= \frac{|S_{B-obj}(f_x,0,f_z)L^3|}{L^2} = L\frac{\kappa_{obj}}{(af_{3D})^{\beta_{obj}}} = \frac{\kappa_{proj}}{(af_{2D})^{\beta_{proj}}}, \quad \text{(A2)}$$

where $f_{2D}=\sqrt{f_x^2+f_z^2}$. The units of S^{2D}_{proj} are equal to those of κ_{proj} (μ^2 mm^2) and the denominator is dimensionless. Comparing to Eq. (A1), we see that β for a projection is equal to that for the object (which is equal to that of the fully 3D image), i.e., $\beta_{proj}=\beta_{obj}$, and the value of κ is scaled by the length of the object being projected, i.e., $\kappa_{proj}=L\cdot\kappa_{obj}$, recognizing the change in units associated with 2D and 3D power spectra.

3. The clutter power spectrum in a 2D slice of the 3D CBCT volume

For a slice through the fully 3D CBCT image, the 2D power spectrum, denoted $S^{2D}_{slice}(f_x,f_z)$, is given by integrating in one direction (taken as f_y) across the 3D Fourier domain, recognizing that 2D and 3D power spectra for the same underlying data have different units.

$$S^{2D}_{slice}(f_x,f_z) = \frac{\left|\int_{-\infty}^{\infty}\tilde{M}^{3D}_{CBCT}(f_x,f_y,f_z)df_y\right|^2}{L^2}$$
$$= \frac{\int\int\tilde{M}^{3D}_{CBCT}(f_x,f_y,f_z)\tilde{M}^{3D*}_{CBCT}(f_x',f_y',f_z')df_y df_y'}{L^2}. \quad \text{(A3a)}$$

The square in the numerator is written as a correlation integral, which by assumption of stationarity, is equal to 0 unless $f_x=f_x'$, $f_y=f_y'$, and $f_z=f_z'$. Therefore, the Fourier transform can be integrated in quadrature as:

$$S^{2D}_{slice}(f_x,f_z) = \frac{\int_{-\infty}^{\infty}|\tilde{M}^{3D}_{CBCT}(f_x,f_y,f_z)|^2df_y}{L^2}df_y'. \quad \text{(A3b)}$$

The increment df_y' can be taken as the inverse of the extent of the object, $1/L$, just as an increment in the spatial domain (the sampling interval) defines the extent of the Fourier domain (the Nyquist region). Therefore,

$$S^{2D}_{slice}(f_x,f_z) = \int_{-\infty}^{\infty}\frac{|\tilde{M}^{3D}_{CBCT}(f_x,f_y,f_z)|^2}{L^3}df_y$$
$$= \int_{-\infty}^{\infty}S_{B-obj}(f_x,f_y,f_z)df_y$$
$$= \int_{-\infty}^{\infty}\frac{\kappa_{obj}}{(af_{3D})^{\beta_{obj}}}df_y$$
$$= \kappa_{obj}[(af_x)^2+(af_z)^2]^{-\beta_{obj}/2} \times\int_{-\infty}^{\infty}\left[1+\frac{(af_y)^2}{[(af_x)^2+(af_z)^2]}\right]^{-\beta_{obj}/2}df_y$$
$$= 2\kappa_{obj}(af_{2D})^{-\beta_{obj}}\int_0^{\infty}\left[1+\frac{(af_y)^2}{(af_{2D})^2}\right]^{-\beta_{obj}/2}df_y. \quad \text{(A3c)}$$

Substituting $\sqrt{(af_y)^2/(af_{2D})^2}$ with p, such that $dp=df_y/f_{2D}$, the slice power spectrum can be written as

$$S^{2D}_{slice}(f_x,f_z) = 2\kappa_{obj}(af_{2D})^{-\beta_{obj}}\int_0^{\infty}[1+p^2]^{-\beta_{obj}/2}(f_{2D}dp)$$
$$= \frac{2\kappa_{obj}}{(af_{2D})^{\beta_{obj}-1}}\int_0^{\infty}[1+p^2]^{-\beta_{obj}/2}dp. \quad \text{(A3d)}$$

The integral is equal to the hypergeometric function, ${}_2F_1(1/2,\beta_{obj}/2;3/2,-p^2)$, evaluated at $p\rightarrow$infinity. We label the value simply as C, which can be evaluated analytically only for a few values of β and is generally evaluated numerically. Thus, S^{2D}_{slice} can be written as:

$$S^{2D}_{slice}(f_x,f_z) = \frac{2C\kappa_{obj}}{(af_{2D})^{\beta_{obj}-1}} = \frac{\kappa_{slice}}{(af_{2D})^{\beta_{slice}}}. \quad \text{(A3e)}$$

The clutter power spectrum for a slice extracted from a 3D image therefore exhibits a value of β reduced by 1 from that of the object and the 3D image, i.e., $\beta_{slice}=\beta_{obj}-1$ and κ is scaled by a constant of order unity which depends on the value of β for the object, i.e., $\kappa_{slice}=2C\kappa_{obj}$.

4. The clutter power spectrum in 3D tomosynthesis

For reconstruction from a limited tomosynthesis arc subtending a "wedge" of angle θ_{tot}, the Fourier domain image is equal to $\tilde{M}_{obj}$ within the wedge, and is zero outside

$$\tilde{M}_{tomo}(f_x,f_y,f_z) = \begin{cases} \tilde{M}_{obj}(f_x,f_y,f_z), |f_y| \le \left|f_x\tan\left(\frac{\theta_{tot}}{2}\right)\right| \\ 0, |f_y| > \left|f_x\tan\left(\frac{\theta_{tot}}{2}\right)\right| \end{cases}. \quad \text{(A4)}$$

The corresponding power spectra are similarly equal within the double-wedge $[S^{3D}_{tomo}(f_x,f_y,f_z)=S_{B-obj}(f_x,f_y,f_z)]$ and 0 outside the wedge. Thus, extraction of a 2D slice from the 3D tomosynthesis image amounts to integration along one dimension (taken as f_y) of the tomosynthesis wedge. The upper limit of the integral in Eq. (A3c) then depends on f_x, and is given by $c=f_x\tan(\theta_{tot}/2)$. When $f_y=c$, we have $p=|c|/\sqrt{f_x^2+f_z^2}=|f_x\tan(\theta_{tot}/2)|/\sqrt{f_x^2+f_z^2}=|\tan(\theta_{tot}/2)\cos(f_\theta)|$, where f_θ is the angle in the (f_x-f_y) plane, measured from the f_x axis. The hypergeometric function is evaluated at this value of p to obtain the factor C in Eq. (A3e), which here depends on θ_{tot}, f_θ, and β_{obj}. This implies that the clutter power spectrum in a 2D slice of a tomosynthesis image does not actually obey the commonly invoked power-law form (even if the object itself consists of power-law fluctuations); furthermore, the 2D slice tomosynthesis power spectrum is nonisotropic (even if the object is isotropic). Special cases exist on the f_x and f_z axes, where the power spectra do obey power-law behavior. Considering power spectra along f_x

(when $f_z=0$) $|\tan(\theta_{tot}/2)\cos(f_\theta)|$ reduces to $|\tan(\theta_{tot}/2)|$ and the hypergeometric function equals a constant independent of f_x and f_z. The magnitude κ of the slice power spectra measured along x depend on θ_{tot} and decrease with angular extent. Along f_z (when $f_x=0$), the hypergeometric function is evaluated at $p=0$, yielding a value of 1. Therefore, as shown in the measurements above, the power spectra on f_x and f_z axes can be fit to power-law curves parametrized by κ and β as a descriptive, empirical characterization of the 2D power spectra.

The tomosynthesis power spectrum exhibits a continuum behavior in θ_{tot}. In one extreme, as θ_{tot} approaches π, p tends to infinity, and the power spectrum of the fully sampled CBCT, described by an isotropic power-law characteristic. In the other extreme, as θ_{tot} approaches zero, the extent of the wedge becomes smaller than $\sim 1/L$. The Fourier components are not independent within this infinitely narrow wedge; rather, they are approximately equal. Integration across this narrow extent should therefore be performed linearly (not in quadrature) as follows:

$$\lim_{\theta\to 0} S^{2D}_{tomo}(f_x,f_z) = \frac{\left|\int_{-c}^{c}\tilde{M}^{3D}_{CBCT}(f_x,f_y,f_z)df_y\right|^2}{L^2} \cong \frac{|\tilde{M}^{3D}_{CBCT}(f_x,0,f_z)2c|^2}{L^2} = \frac{|\tilde{M}^{3D}_{CBCT}(f_x,0,f_z)2f_x\tan(\theta_{tot}/2)|^2}{L^2}. \quad \text{(A5a)}$$

Using the small angle approximation $\tan(\theta_{tot}/2)\cong(\theta_{tot}/2)$, and $\theta_{tot}=\Delta\theta\cdot N_{proj}$ with $N_{proj}=1$, we have

$$\lim_{\theta\to 0} S^{2D}_{tomo}(f_x,f_z) \cong \frac{|\tilde{M}^{3D}_{CBCT}(f_x,0,f_z)|^2}{L^2}(f_x\theta_{tot})^2 = \frac{S^{3D}_{CBCT}(f_x,0,f_z)L^3}{L^2}(f_x\theta_{tot})^2 = S^{3D}_{CBCT}(f_x,0,f_z)L(f_x\Delta\theta)^2, \quad \text{(A5b)}$$

which is the power spectrum for a single filtered projection. The term $S^{3D}_{CBCT}(f_x,0,f_z)L$ is the power spectrum of a projection, and $(f_x\theta_{tot})^2$ is the square of the ramp filter. In retrospect, this is not a surprising result: Ramp filtered projections approximating double-wedges in Fourier space are simply the basis of filtered backprojection.[51]

APPENDIX B: CALCULATION OF THE POWER SPECTRUM AS A DISCRETE SUM OVER (FEW) PROJECTIONS

When the angular increment between projections is large, (e.g., large tomosynthesis angle and small N_{proj}), the transfer function of backprojection in CBCT does not approximate a radially symmetric, continuous function of $\sim 1/f_{2D}$.[25] Therefore, the contribution of each projection to the signal and noise transfer characteristics must be added explicitly. As illustrated in Fig. 9, three frequency regions are proposed for numerical approximation.

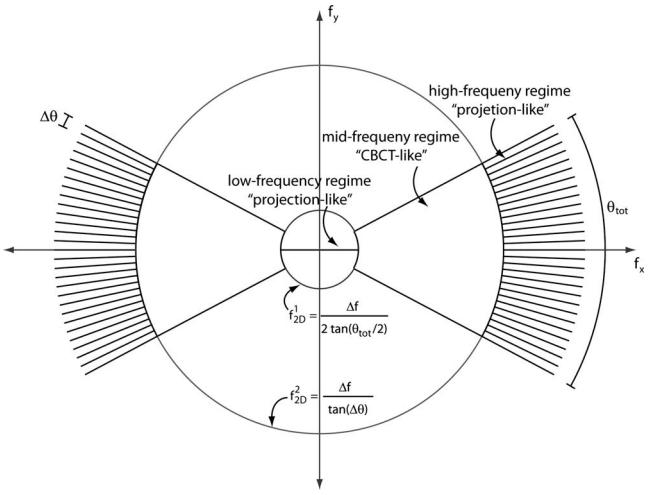

FIG. 9. Three regions of the Fourier domain relevant to computing detectability for few projections covering a wide source-detector arc are identified and the boundary frequencies are labeled.

Region (1) is the low-frequency regime bounded by the radius at which the sampled double-wedge becomes wider than the discrete frequency increment Δf (given by the reciprocal of the extent of the ROI)

$$f^1_{2D} = \frac{\Delta f}{2\tan\left(\frac{\theta_{tot}}{2}\right)}. \quad \text{(B1)}$$

Within region (1), projections are closely spaced such that each vane adds nearly on top of the previous, approximately equivalent to summing over N_{proj} projections at the same angle. Detectability index in this region is given by

$$d'^2_1 = \int\int \frac{N^2_{proj}G^2\mathrm{MTF}^2(f_x,f_z)}{N^2_{proj}S_{B-proj}(f_x,f_z) + N_{proj}[S_Q(f_x,f_z)+S_E(f_x,f_z)]}\cdot|\Delta H(f_x,f_z)|^2 df_x df_z, \quad \text{(B2)}$$

where G is the gain factor associated with projection as defined in previous work,[25,52] and $S_{B-proj}(f_x,f_z)$ is the power spectrum presented on a projection, given by $S_{B-proj}(f_x,f_z) = G^2L\mathrm{MTF}^2(f_x,f_z)\kappa_{obj}/(af_{2D})^{\beta_{obj}}$, with L denoting the length of the anatomical clutter projected through.

Region (2) is the midfrequency regime bounded by Eq. (B1) and the angular Nyquist criterion

$$f^2_{2D} = \frac{\Delta f}{\tan(\Delta\theta)}, \quad \text{(B3)}$$

where projections are close enough to approximate a continuum similar to a fully sampled CBCT scan. Detectability index is given by

$$d_2'^2 = \int\int\int \frac{\mathrm{MTF}^2(f_x,f_y,f_z)}{S_B(f_x,f_y,f_z) + S_Q(f_x,f_y,f_z) + S_E(f_x,f_y,f_z)} \cdot |\Delta H(f_x,f_y,f_z)|^2 df_x df_y df_z. \quad \text{(B4)}$$

Finally, region (3) is the high-frequency regime, where projections are far apart and each projection contributes to detectability index independently

$$d_3'^2 = N_{\mathrm{proj}} \int\int \frac{N_{\mathrm{proj}}^2 \mathrm{MTF}^2(f_x,f_z)}{S_{B-\mathrm{proj}}(f_x,f_z) + S_Q(f_x,f_z) + S_E(f_x,f_z)} \cdot |\Delta H(f_x,f_z)|^2 df_x df_z. \quad \text{(B5)}$$

The overall detectability index is then given by

$$d'^2 = d_1'^2 + d_2'^2 + d_3'^2, \quad \text{(B6)}$$

where, for simplicity, the task function is assumed to be radially symmetric, and the NPS and MTF are taken to be appropriate for either a filtered projection image or a CBCT image.

The major difference in contribution to detectability from the "projectionlike" regions versus the "CBCT-like" region is the factor L in the denominator. It has been previously shown that the need to optimize a 3D imaging system relies on understanding of 3D noise aliasing (which prevents deterministic filters from canceling out in the detectability index), and optimization of the projections alone is not sufficient.[52] This analysis shows that clutter contributes differently to detectability in 3D images than in projections, and therefore presents another compelling reason why a 3D imaging system must be optimized based on the 3D signal and noise characteristics.

[a]Author to whom correspondence should be addressed. Electronic mail: jeff.siewerdsen@jhu.edu; Telephone: 443-287-6269.

[1]F. O. Bochud, J. F. Valley, F. R. Verdun, C. Hessler, and P. Schnyder, "Estimation of the noisy component of anatomical backgrounds," Med. Phys. **26**(7), 1365–1370 (1999).
[2]F. O. Bochud, F. R. Verdun, J. F. Valley, C. Hessler, and R. Moeckli, "The importance of anatomical noise in mammography," Proc. SPIE **3036**, 74–80 (1997).
[3]E. Samei, M. J. Flynn, and W. R. Eyler, "Detection of subtle lung nodules: Relative influence of quantum and anatomic noise on chest radiographs," Radiology **213**(3), 727–734 (1999).
[4]E. Samei, W. R. Eyler, and L. Baron, *Effects of Anatomical Structure on Signal Detection* (SPIE Publications, Washington, 2000); J. Beutel, H. L. Kundel, and R. L. Van Metter, *Handbook of Medical Imaging: Physics and Psychophysics* (SPIE Publications, Washington, 2000), Vol. 1, Chap. 12, pp. 655–682.
[5]H. L. Kundel, C. F. Nodine, D. Thickman, D. Carmody, and L. Toto, "Nodule detection with and without a chest image," Invest. Radiol. **20**(1), 94–99 (1985).
[6]U. E. Ruttimann and R. L. Webber, "A simple model combining quantum noise and anatomical variation in radiographs," Med. Phys. **11**(1), 50–60 (1984).
[7]J. S. Whiting, M. Eckstein, C. A. Morioka, and N. L. Eigler, "Effect of additive noise, signal contrast and feature motion on visual detection in structured noise," Proc. SPIE **2712**, 26–38 (1996).
[8]P. F. Judy, R. G. Swensson, R. D. Nawfel, K. H. Chan, and S. E. Seltzer, "Contrast-detail curves for liver CT," Med. Phys. **19**(5), 1167–1174 (1992).
[9]H. H. Barrett, "Objective assessment of image quality: Effects of quantum noise and object variability," J. Opt. Soc. Am. A **7**(7), 1266–1278 (1990).
[10]E. Samei, M. J. Flynn, E. Peterson, and W. R. Eyler, "Subtle lung nodules: Influence of local anatomic variations on detection," Radiology **228**(1), 76–84 (2003).
[11]G. Revesz, H. L. Kundel, and M. A. Graber, "The influence of structured noise on the detection of radiologic abnormalities," Invest. Radiol. **9**(6), 479–486 (1974).
[12]J. T. Dobbins III and D. J. Godfrey, "Digital x-ray tomosynthesis: Current state of the art and clinical potential," Phys. Med. Biol. **48**(19), R65–R106 (2003).
[13]J. T. Dobbins III, H. P. McAdams, D. J. Godfrey, and C. Li, "Digital tomosynthesis of the chest," J. Thorac. Imaging **23**(2), 86–92 (2008).
[14]A. E. Burgess, "Mammographic structure: Data preparation and spatial statistics analysis," Proc. SPIE **3661**, 642–653 (1999).
[15]A. E. Burgess, F. L. Jacobson, and P. F. Judy, "Human observer detection experiments with mammograms and power-law noise," Med. Phys. **28**(4), 419–437 (2001).
[16]J. J. Heine, S. R. Deans, R. P. Velthuizen, and L. P. Clarke, "On the statistical nature of mammograms," Med. Phys. **26**(11), 2254–2265 (1999).
[17]J. J. Heine and R. P. Velthuizen, "Spectral analysis of full field digital mammography data," Med. Phys. **29**(5), 647–661 (2002).
[18]S. Richard, J. H. Siewerdsen, D. A. Jaffray, D. J. Moseley, and B. Bakhtiar, "Generalized DQE analysis of radiographic and dual-energy imaging using flat-panel detectors," Med. Phys. **32**(5), 1397–1413 (2005).
[19]S. Richard and J. H. Siewerdsen, "Optimization of dual-energy imaging systems using generalized NEQ and imaging task," Med. Phys. **34**(1), 127–139 (2007).
[20]S. J. Glick, S. Vedantham, and A. Karellas, "Investigation of optimal kVp setting for CT mammography using a flat-panel imager," Proc. SPIE **4682**, 392–402 (2002).
[21]X. Gong, S. J. Glick, B. Liu, A. A. Vedula, and S. Thacker, "A computer simulation study comparing lesion detection accuracy with digital mammography, breast tomosynthesis, and cone-beam CT breast imaging," Med. Phys. **33**(4), 1041–1052 (2006).
[22]K. G. Metheany, C. K. Abbey, N. Packard, and J. M. Boone, "Characterizing anatomical variability in breast CT images," Med. Phys. **35**(10), 4685–4694 (2008).
[23]E. Engstrom, I. Reiser, and R. Nishikawa, "Comparison of power spectra for tomosynthesis projections and reconstructed images," Med. Phys. **36**(5), 1753–1758 (2009).
[24]S. Yoon, J. G. Gang, D. J. Tward, J. H. Siewerdsen, and R. Fahrig, "Analysis of lung nodule detectability and anatomical clutter in tomosynthesis imaging of the chest," Proc. SPIE **7258**, 72581M–72581M-11 (2009).
[25]D. J. Tward and J. H. Siewerdsen, "Cascaded systems analysis of the 3D noise transfer characteristics of flat-panel cone-beam CT," Med. Phys. **35**(12), 5510–5529 (2008).
[26]M. Schroeder, *Fractals, Chaos, Power Laws: Minutes from an Infinite Paradise* (Freeman, New York, 1992).
[27]J. D. Murray, *Mathematical Biology II: Spatial Models and Biomedical Applications* (Springer-Verlag, Berlin, 2003), pp. 490–496.
[28]S. Richard and J. H. Siewerdsen, "Cascaded systems analysis of noise reduction algorithms in dual-energy imaging," Med. Phys. **35**(2), 586–601 (2008).
[29]S. Richard and J. H. Siewerdsen, "Comparison of model and human observer performance for detection and discrimination tasks using dual-energy x-ray images," Med. Phys. **35**(11), 5043–5053 (2008).
[30]J. H. Siewerdsen, A. M. Waese, D. J. Moseley, S. Richard, and D. A. Jaffray, "Spektr: A computational tool for x-ray spectral analysis and imaging system optimization," Med. Phys. **31**(11), 3057–3067 (2004).
[31]D. L. Parker, "Optimal short scan convolution reconstruction for fanbeam CT," Med. Phys. **9**(2), 254–257 (1982).
[32]M. D. Silver, "A method for including redundant data in computed tomography," Med. Phys. **27**(4), 773–774 (2000).
[33]K. M. Hanson, "Detectability in computed tomographic images," Med. Phys. **6**(5), 441–451 (1979).
[34]J. H. Siewerdsen, I. A. Cunningham, and D. A. Jaffray, "A Framework for noise-power spectrum analysis of multidimensional images," Med. Phys. **29**(11), 2655–2671 (2002).
[35]J. Neter, M. Kutner, W. Wasserman, and C. Nachtsheim, *Applied Linear Statistical Models* (McGraw-Hill/Irwin, New York, 2009), Vol. 4.
[36]D. J. Tward and J. H. Siewerdsen, "Noise aliasing and the 3D NEQ of flat-panel cone-beam CT: Effect of 2D/3D apertures and sampling," Med. Phys. **36**(8), 3830–3843 (2009).
[37]J. Yao and I. A. Cunningham, "Parallel cascades: New ways to describe

noise transfer in medical imaging systems," Med. Phys. **28**(10), 2020–2038 (2001).
[38]International Commission on Radiation Units and Measurements, "Medical imaging—The assessment of image quality," ICRU Report No. 54 (International Commission on Radiation Units and Measurements, Bethesda, MD, 1996).
[39]J. H. Siewerdsen, L. E. Antonuk, Y. El Mohri, J. Yorkston, W. Huang, and I. A. Cunningham, "Signal, noise power spectrum, and detective quantum efficiency of indirect-detection flat-panel imagers for diagnostic radiology," Med. Phys. **25**(5), 614–628 (1998).
[40]J. H. Siewerdsen, L. E. Antonuk, Y. El Mohri, J. Yorkston, W. Huang, J. M. Boudry, and I. A. Cunningham, "Empirical and theoretical investigation of the noise performance of indirect detection, active matrix flat-panel imagers (AMFPIs) for diagnostic radiology," Med. Phys. **24**(1), 71–89 (1997).
[41]H. H. Barrett, J. P. Rolland, R. F. Wagner, and K. J. Myers, "Detection and discrimination of known signals in inhomogeneous, random backgrounds," in Proceedings of the SPIE Medical Imaging III: Image Formation, 1989, Vol. 1090, pp. 176–182.
[42]K. Taguchi, "Temporal resolution and the evaluation of candidate algorithms for four-dimensional CT," Med. Phys. **30**(4), 640–650 (2003).
[43]S. Bartolac, R. Clackdoyle, F. Noo, J. Siewerdsen, D. Moseley, and D. Jaffray, "A local shift-variant Fourier model and experimental validation of circular cone-beam computed tomography artifacts," Med. Phys. **36**(2), 500–512 (2009).
[44]A. E. Burgess and P. F. Judy, "Signal detection in power-law noise: Effect of spectrum exponents," J. Opt. Soc. Am. A Opt. Image Sci. Vis. **24**(12), B52–B60 (2007).
[45]B. Zhao and W. Zhao, "Three-dimensional linear system analysis for breast tomosynthesis," Med. Phys. **35**(12), 5219–5232 (2008).
[46]T. Wu, A. Stewart, M. Stanton, T. McCauley, W. Phillips, D. B. Kopans, R. H. Moore, J. W. Eberhard, B. Opsahl-Ong, L. Niklason, and M. B. Williams, "Tomographic mammography using a limited number of low-dose cone-beam projection images," Med. Phys. **30**(3), 365–380 (2003).
[47]J. D. Sain and H. H. Barrett, "Performance evaluation of a modular gamma camera using a detectability index," J. Nucl. Med. **44**(1), 58–66 (2003).
[48]J. Y. Hesterman, M. A. Kupinski, E. Clarkson, and H. H. Barrett, "Hardware assessment using the multi-module, multi-resolution system (M3R): A signal-detection study," Med. Phys. **34**(7), 3034–3044 (2007).
[49]S. Park, H. Liu, R. Jennings, R. Leimbach, I. Kyprianou, A. Badano, and K. Myers, "A task-based evaluation method for x-ray breast imaging systems using variable-background phantoms," Proc. SPIE **7258**, 72581L–72581L-9 (2009).
[50]A. Badal, L. Kyprianou, D. P. Banh, A. Badano, and J. Sempau, "PenMesh—Monte Carlo radiation transport simulation in a triangle mesh geometry," IEEE Trans. Med. Imaging **28**(12), 1894–1901 (2009).
[51]A. C. Kak and M. Slaney, *Principles of Computerized Tomographic Imaging* (Society for Industrial Mathematics, New York, 2001).
[52]D. J. Tward, J. H. Siewerdsen, R. A. Fahrig, and A. R. Pineda, "Cascaded systems analysis of the 3D NEQ for cone-beam CT and tomosynthesis," Proc. SPIE **6913**, 69131S–69131S-12 (2008).